UNIVERSITY OF TARTU

Faculty of Science and Technology

Institute of Chemistry

Chair of Physical Chemistry

Paul Erik Olli

Photoelectrocatalytic Hydrogen Generation at Photocathode Based on Silicon Nanowires Grown from Alternative Seeds

Bachelor's thesis (12 ECTS)

Chemistry

Supervisors: Pascale Chenevier, PhD

(Commissariat à l'énergie atomique et aux énergies alternatives, Grenoble)

Jaak Nerut, PhD (University of Tartu)

Tartu 2024

Abstract

Photoelectrocatalytic Hydrogen Generation at Photocathode Based on Silicon Nanowires Grown from Alternative Seeds

The aim of the study was to explore alternative growth seeds to gold nanoparticles for the synthesis of silicon nanowires (SiNWs), characterise the SiNWs grown from alternative seeds, create a water splitting photocathode based on SiNWs, and evaluate the photoelectrocatalytic performance of the photocathode. Quantum dots were synthesised and used as alternative seeds for the SiNWs, which were grown on an amorphous carbon substrate. Scanning electron microscopy estabished the sizes and shapes of the nanowires. Every constituent metal of quantum dots was attributed to a specific morphological characteristic of the nanowires. The kinetics of SiNW growth on alternative seeds was evaluated. Catalyst electrodeposition proved the be the best catalyst application method. Photocathode with SiNWs from alternative seeds was found to be inferior to the photocathode with SiNWs grown from gold nanoparticles. Alternative growth seeds proved to be suitable and of interest for growing SiNWs.

Keywords: Silicon nanowires, quantum dots, photoelectrocatalysis, hydrogen, molybdenum sulphide catalyst

CERCS: P401 Electrochemistry, T150 Material technology, T140 Energy research

Vesiniku fotoelektrokatalüüs alternatiivsetest kristallatsioonitsentritest kasvatatud räni-nanotraatidel põhineval fotokatoodil

Uurimistöö eesmärk oli leida alternatiivseid kristalliatsioonitsentreid kulla nanoosakestele räni-nanotraatide (RNT) sünteesiks, karakteriseerida alternatiivsetetest kristallatsioonitsentritest kasvatatud RNTe, luua RNTdel põhinev vee lõhustamise fotokatood ning hinnata fotokatoodi elektrokeemililist võimekust. Alternatiivsete kristallasioonitsentritena kasutati sünteesitud kvanttäppe, et kasvatada nendest RNTe poorsele süsinikkandjale. Skaneeriva elektronmikroskoobiga määrati räni RNTde suurus ja kuju. Analüüsiti, millist mõju avaldab RNTide kujule iga kvanttäppide koostises olev metall. Hinnati RNTde kasvu kineetikat alternatiivsetel kristallatsioonitsentritel. Katalüsaatori elektrosadestamine andAlternatiivsetest kristallatsioonitsentritest RNTidel põhinev fotokatood oli väiksema fotovooluga kui kulla nano-osakestest kasvatatud räni-nanotraatidel põhinev fotokatood. Alternatiivsed kristallatsioonitsentrid on sobilikud ja atraktiivne valik RNTde kasvatamiseks.

Märksõnad: Räni nanotraadid, kvanttäpid, fotoelektrokeemia, vesinik, molübdeensulfiid katalüsaator

CERCS: P401 Elektrokeemia, T150 Materjalitehnoloogia, T140 Energeetika

Table of contents

Abbreviations

CIS – $CuInS_2$

CIZS – CuInZnS

CVD – chemical vapour deposition

GDL – gas diffusion layer

GSH – L-gluthathione

LSV – linear sweep voltammetry

RHE – reversible hydrogen electrode

SEM – scanning electron microscope

SEM-EDX – scanning electron microscopy with energy dispersive X-ray spectroscopy

SHE – standard hydrogen electrode

SiNW – silicon nanowire

UV-VIS – ultraviolet-visible spectroscopy

VLS – vapour-liquid-solid

Introduction

The commercial feasibility of laboratory hydrogen photoelectrocatalysis concepts has long been a dream. A photoelectrochemical device capable of generating an inexhaustible amount of hydrogen with no other energy input than solar irradiance could be the key to addressing humanity's need for clean energy. However, the realisation of this concept has been hindered by inefficiency and practical difficulties. Ever since Fujishima and Honda first described the photolysis of water on TiO_2 nanoparticles [1], scientists have been making strides towards enabling large-scale photoelectrochemical generation.

A water-splitting photoelectrochemical device consists of a photocathode, where hydrogen evolution occurs, and a photoanode, where water oxidation occurs. This work investigates hydrogen generation on a photocathode based on silicon nanowires coated with amorphous molybdenum sulphide. Silicon acts as a semiconductor, absorbing solar irradiance and creating electron-hole pairs necessary for hydrogen evolution. The morphology of nanowires offers a large surface area, porosity necessary for hydrogen gas transport, as well as enhanced photon absorption properties thanks to quantum effects.

Silicon nanowires are grown on a porous carbon substrate using chemical vapour deposition method, where diphenylsilane decomposes to silicon on nano-sized seeds. Although tin sulphide, gold, and various metal seeds have been successfully used before to grow silicon nanowires for lithium-ion batteries and photocathodes [2–4], this work explores the use of quantum dots as alternative bi- and tri-metal sulphide nanoparticles for growing silicon nanowires to combine the properties of different metals into one seed.

Silicon nanowires are coated with amorphous molybdenum sulphide catalyst [5], which serves as an inexpensive alternative to conventional noble-metal catalysts, like platinum [6], to aid hydrogen evolution. The photocathodes are assessed by measuring photocurrent produced by irradiating the photocathode with the sunlight spectrum.

The aims of this thesis were:

1) To explore various growth seeds to replace gold nanoparticles for silicon nanowire synthesis using diphenylsilane decomposition chemical vapour deposition method.
2) To charaterise the silicon nanowires grown using alternative growth seeds.
3) To evaluate the photoelectrocatalytic performance of the photocathode based on silicon nanowires grown using alternative seeds and coated with amorphous molybdenum sulphide catalyst.

1. Literature review

1.1. Hydrogen as the key energy carrier in future energy economy

Nowadays, global warming is the driving factor for the swift change of the energy economy. The world has heavily relied on fossil fuels, such as coal, oil, and natural gas, to fill its primary energy needs. However, greenhouse gases, mainly CO_2, emitted from the use of fossil fuels cause global warming which in turn increase the frequency and magnitude of extreme weather conditions [7,8]. Industries and governments are now actively working towards decarbonisation – replacing fossil energy sources with renewable ones.

Green energy is the successor to fossil fuels with the most common form being green electricity. However, green electricity suffers from temporal and regional stability based on weather conditions, cannot be directly used for many currently carbon intense processes, such as cement and steel production, and transportation. These drawbacks have introduced new challenges and proved that the transition to green energy is not as simple as building fields of wind turbines. Many of these challenges can be solved by introducing green hydrogen produced from carbon free sources as the central energy carrier of the energy economy.

1.1.1. Hydrogen applications

First of hydrogen's advantages is its high specific energy, 33.3 kWh kg^{-1} (Lower heating value) compared to 12.8 kWh kg^{-1} for traditional petrol. Albeit often titled the energy carrier of the future, it has already been extensively used irreplaceably, the most notable being the production of ammonia, the basis for fertilisers, by the Haber-Bosch process. In 2008, Erisman et al concluded that 48% of world's population's existence was made possible by the food provided by nitrogen fertilisers from Haber-Bosch process [9]. Other important applications for hydrogen are oil refining, the production of methanol, hydrogenation of food products, rocket fuel, and a myriad of different processes in the chemical industry.

Hydrogen is gaining attention for its potential uses. It can power transportation through fuel cells, emitting only water, thus eliminating carbon emissions and local air pollution. As vehicle weight increases, hydrogen becomes more advantageous than batteries, which become impractical due to their increasing weight [10]. Hydrogen's high specific energy makes it suitable for heavy transport like trains, planes, and ships [11]. Additionally, hydrogen can balance the green electricity grid, being produced using water electrolysis during electricity surplus and generating electricity using fuel cells during electricity shortages.

In industry, green hydrogen holds great potential for decarbonising steel production, a sector responsible for 7% of global CO2 emissions in 2014 due to coal use in the conventional production technology to reduce iron oxide [12]. Substituting coal with hydrogen in iron ore reduction could nearly eliminate carbon emissions [13]. Similarly, the cement industry, which contributes 7% to global CO2 emissions, could reduce its manufacturing process's emissions by 27.6% by replacing fossil fuels with hydrogen [12,14] The remaining emissions stem from limestone decomposition [14].

Hydrogen can also be used to produce e-fuels, such as methane, methanol and ammonia, through carbon dioxide or nitrogen hydrogenation [15]. This allows for the continued use of conventional vehicles and already built infrastructure without emissions. Finally, hydrogen is replacing supplementing natural gas for domestic use in landline pipelines. This is already being implemented in the United Kingdom [16].

However, producing, storing and handling hydrogen has challenges that have impeded the transition. Albeit possessing the highest specific energy, hydrogen, being a very light gas, has a very low volumetric energy density. For means of practical transportation other than pipelines it requires compression or liquefication, which require energy accounting for 20% and 30% of hydrogen's energy content, respectively [17]. Novel means of hydrogen storage, such as complex hydrides are being investigated [18], but only conventional compression and liquefication are currently commercially used.

The second issue is safety due to hydrogen being a highly flammable gas. In air, hydrogen's is explosive limits are between 18 and 59% and its flammability limits are between 4 and 74% [19]. Fortunately, hydrogen quickly disperses in the atmosphere and reaching these ratios is unlikely. Finally, the current cost of producing green hydrogen is high. Green hydrogen is mainly produced using electrolysers that require extensive amounts of green electricity, which is not yet excessively abundant. Moreover, building additional infrastructure, such as production equipment, pipelines etc, introduces additional capital expenditure [10].

1.2. Green hydrogen production

Not all hydrogen is created equal. Hydrogen is often color-coded to distinguish its production method. Conventional grey hydrogen is produced from natural gas through steam methane reforming. Currently, grey hydrogen accounts for 97% of produced hydrogen and carries a heavy carbon footprint. Naturally, abovementioned decarbonisation opportunities are not possible with grey hydrogen. However, the energy carrier of the future is green hydrogen, which is produced from renewable sources, typically through electrolysis.

1.2.1. Hydrogen production by electrolysis

Electrolysis is currently the main technology for producing green hydrogen. Electrolysis devices utilise green electricity for electrochemical water splitting. Three main technologies are alkaline electrolysis, proton-exchange membrane electrolysis and solid oxide electrolysis. The respective electricity to hydrogen conversion efficiency ranges are 62-82%, 67-82%, and 81-86% [15]. If an electrolyser is using electricity from solar cells, and considering the typical 20% efficiency of a photovoltaic, an average 75% electrolyser would have 15% solar to hydrogen conversion efficiency, not considering any other possible losses.

1.2.2. Photoelectrochemical water splitting

Photoelectrochemical water splitting is a method aiming to convert the production steps from primary energy to green hydrogen into one process. Compared to electrolysis driven by photovoltaics photoelectrochemical water splitting device has the potential benefit of improved efficiency thanks to lower overpotential required to drive the reaction, resulting in higher solar to hydrogen efficiency, reduced cost of infrastructure, and safer operation [19]. Photoelectrochemical water splitting device converts water to oxygen and hydrogen at separate electrodes. A distinction has to be made from photocatalytic device, where both gases are generated in a single aqueous system with a suspended semiconductor powder, requiring subsequent gas separation [19,20].

The water splitting reaction (1) has Gibbs free energy of 1.23 eV, translating to 1008 nm wavelength photon. Therefore, solar spectrum photons, ranging from 1 eV to 3 eV, have sufficient energy to initiate the reaction [19].

$$2H_2O \rightarrow 2H_2 + O_2 \quad (1)$$

Since water is transparent to visible light, a mediator is necessary to utilise the solar energy. Semiconductors are used to convert solar irradiance to chemical potential [1,20–23]. Photons excite electrons from conduction band to balance band creating electron-hole pairs which drive either reduction or oxidation, depending on the absolute potential. The difference between conduction and valence band potential is referred to as band gap, which determines the energy of electron-hole pairs and the wavelengths material can absorb.

In addition to sufficient energy, the band gap positions determine the reactions the electron-hole pairs can drive. An ideal material for photocatalytic water-splitting would have conduction band potential more negative than the reduction potential of protons and valence band more positive than oxidation potential of water (**Figure 1**) [24].

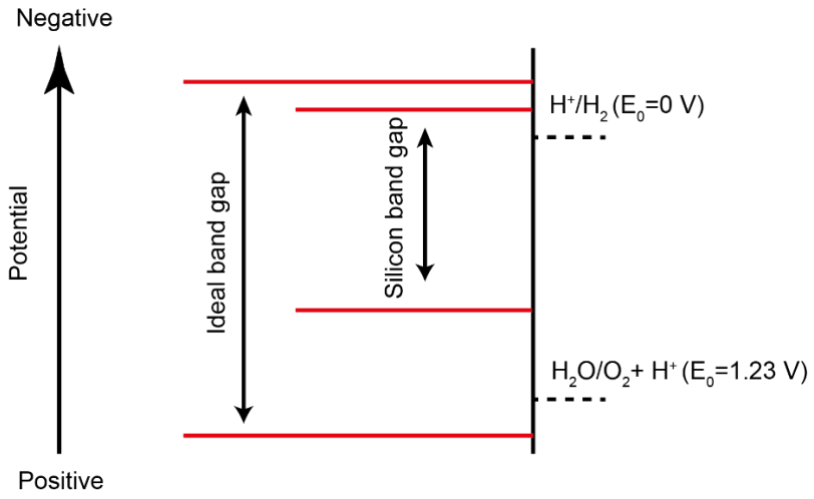

Figure 1. The band gap energies required for water splitting. Semiconductor with an ideal band gap can drive the water splitting reaction. Silicon's band gap is sufficient to drive the hydrogen evolution half-reaction.

Alternatively, the half-reactions can be driven on two separate materials. Photocathode can drive the hydrogen evolution (2) and photoanode the oxidation of water (3), which is in combination is photoelectrochemical water splitting. Silicon has a 1.14 eV band gap of and band gap position suitable for hydrogen evolution reaction [22].

$$2H^+ + 2e^- \rightarrow H_2 \quad (2)$$

$$2H_2O \rightarrow O_2 + 4\,H^+ + 4e^- \quad (3)$$

The most efficient types of cells have been tandem or z-scheme cells, where two semiconductors are employed jointly in a series to drive a reaction. This enables the use of small band gap semiconductors, which absorb a wider range of solar spectrum [25]. Even though the same in principle, tandem cells are employed in photoelectrochemical systems and z-scheme is employed in photocatalysis systems. Silicon could potentially be one semiconductor of a tandem photoelectrochemical system.

1.2.3. Hydrogen evolution cocatalysts and electrode passivators

The semiconductors are supplemented with cocatalysts to minimise the overpotentials associated with the electron transfer of protons in aqueous medium [26,27]. Noble metals such as Pt, Pd and Ru have been investigated on silicon for hydrogen evolution [6,28–30]. However, in large-scale applications noble metals are too costly. For this reason, part of research has shifted towards finding more sustainable alternatives like amorphous MoS_x, which is also used in this work [5,31,32]. Although MoS_x-based photocathode achieved only 11 mA cm^{-2} at 0 V vs regular hydrogen electrode (RHE) compared to the 30 or 37 mA cm^{-2} reached by platinum and ruthenium catalysts respectively, the underlying electrode materials on which the catalyst was deposited were not identical [27,32,33]. In addition, it has been concluded that with proper

engineering approaches there are pathways to approach Pt-level activity with molybdenum sulphide [31].

Electrodes are often multi-layered, and passivators are used to protect the underlying photocathode semiconductor materials from oxidation and to reduce carrier recombination. Commonly used materials are TiO_2 and Al_2O_3, the latter of which having been also employed on silicon. [26,27,32,34]

1.2.4. Nanostructured photoelectrodes

Nanostructured photoelectrodes have numerous benefits. Firstly, shortened carrier collection path from the spot of photoexcitation to the interface where reaction occurs. Secondly, nanostructures improve horizontal light distribution thanks to light scattering. This improves absorption because photons that would otherwise be reflected is scattered around nanostructures and more opportunities to be absorbed. Thirdly, due to quantum confinement effects, decreasing nanoparticle size increases band gap width. Increased surface area also increases charge transfer between interfaces and provides more available reaction centres, requiring lower overpotentials to reach the onset potential of kinetically slow water redox reactions. In addition, due to small size of the nanostructures, the external electric field of ions can be used to alter potential inside the nanostructure. And finally, size-confined nanocrystals enable multiple exciton generation where a photon with an energy *n* times the band gap of the nanocrystal creates *n* electron-hole pairs upon absorption in the crystal. [25]

Nanostructures often offer greater photocurrent compared to planar counterparts. Lee et al. created a photocathode with InP nanopillars, TiO_2 passivator and Ru catalyst which achieved photocurrent 37 mA cm^{-2} at 0 V vs RHE compared to 27 mA cm^{-2} for planar InP counterpart. Furthermore, the maximum hydrogen production efficiency at an applied bias relative to a perfect anode was 14%. [27]

1.3. Silicon nanowires

Silicon nanowires (SiNWs) are wire-like nanostructures of silicon ranging from a few nanometers to a micrometer in diameter. SiNWs have many prospective applications such as Li-ion battery anode material, chemical gas sensors, nanoscale electronic devices, photovoltaics, supercapacitors and biosensors [2,35–39].

SiNWs can be synthesised through various techniques. The main methods are chemical vapour deposition (CVD) a synonym for vapour-liquid-solid (VLS) deposition in this context,

reactive ion-etching, metal-assisted chemical etching, laser ablation, evaporation of SiO and molecular beam epitaxy (MBE) [4,40].

1.3.1. Chemical vapour deposition method

Chemical vapour deposition is an established method for growing silicon crystals from seeds that was first used in 1964 with gold nanoparticles as the seed. The metal nanoparticles (seeds) melt upon heating, and gaseous silicon precursors such as $SiCl_4$ or silane, will decompose on the surface of the seed, forming a liquid metal-Si alloy. After reaching the eutectic phase and crossing the liquidus line of liquid phase and solid-silicon-molten-gold phase, the liquid becomes saturated of silicon, and the silicon begins to crystallise out from the droplet in a certain direction. The continuation of this process results in silicon nanowires. [4,41,42]

Although Au has been the most common catalyst successful SiNWs synthesis has been done with many different metals including Ag, Al, Cu, Ga, In, and Zn [4]. However, tuning the size of SiNWs with metallic nanoparticle seeds is difficult. To replace metals, this work is looking towards organometallic molecules with easily tuneable sizes that would decompose in the heating process.

Tin sulphide is the only sulphide that has been successfully explored before. Tin sulphide decomposes, emitting hydrogen sulphide in the process. In contrast to oxygen, sulphide does not incorporate into silicon. [2]

1.4. Quantum dots

Quantum dots are semiconductor particles of nanoscale size that exhibit quantum effects. These effects emerge as electron or hole is confined to a size comparable to its De Broglie wavelength. As a result, electrons and holes exhibit discrete density of states like in atoms. [43]

Quantum dots have a wide and continuous excitation spectrum while the emission spectrum is narrow and symmetrical. As an intermediary between an atom and a bulk material, the band gap of quantum dots can be tuned by controlling the size of the particle. As the quantum dots shrink, the band gap increases, and the photoluminescence spectrum exhibits a blue shift. Altering the composition and size of the quantum dots, the emission spectrum can be tuned to the desired shape and intensity from ultraviolet to infrared wavelengths. The surface of quantum dots is usually passivated using ligands such as oleic acid or oleyamine to protect the nanoparticle from environmental degradation and render them colloidally stable. Quantum dots have a myriad of applications such as biosensors, drug delivery, cameras, displays, illumination, photovoltaic cells and many more. [43,44]

In this study, sulphide quantum dots are employed as the seeds for the synthesis of SiNWs. The use of quantum dots as the seeds offers advantages such as the ability to easily modify the alloy composition and precisely tune the size.

2. Experimental

2.1. Synthesis of nanoparticles for the growth of silicon nanowires

Synthesis was carried out in a three-necked flask with a vertical condenser (**Figure 2**). The used reagents are specified in Supplementary 2. An inert gas environment was provided by a flow of argon exiting from a bubbler and entering from the top of the vertical condenser, except for gold nanoparticles (AuNPs) synthesised in an air environment. Solubilised reagents were inserted with a metal syringe through a rubber septum, except for AuNP synthesis where Teflon tubes were utilised. When noted, the dissolution was assisted using the VWR 45 kHz 30 W ultrasonic bath. Quantum dot reaction flasks were heated in a water bath (**Figure 2a**), and AuNPs in an oil bath placed on a hot plate (**Figure 2b**). The reaction mixtures were constantly agitated throughout the reaction procedure with a magnetic stirrer. The acidity of the reaction mixture was measured using indicator paper.

Synthesised quantum dots were purified by creating a 1:1 to 1:1.5 v:v ratio of water and propan-2-ol in a 50 mL falcon tube, and centrifugating the mixture at 8500 rpm for 10 minutes in Eppendorf Centrifuge 5804, except when noted differently. By-products of synthesis remained in the supernatant, and quantum dots precipitated in the bottom of the tube. Centrifugation was done in several falcons or multiple times if required by the volume of the product or the difficulty of precipitation. The transparent supernatant was disposed and the remaining solvent dried at room temperature in argon flow to weigh the mass of the quantum dots.

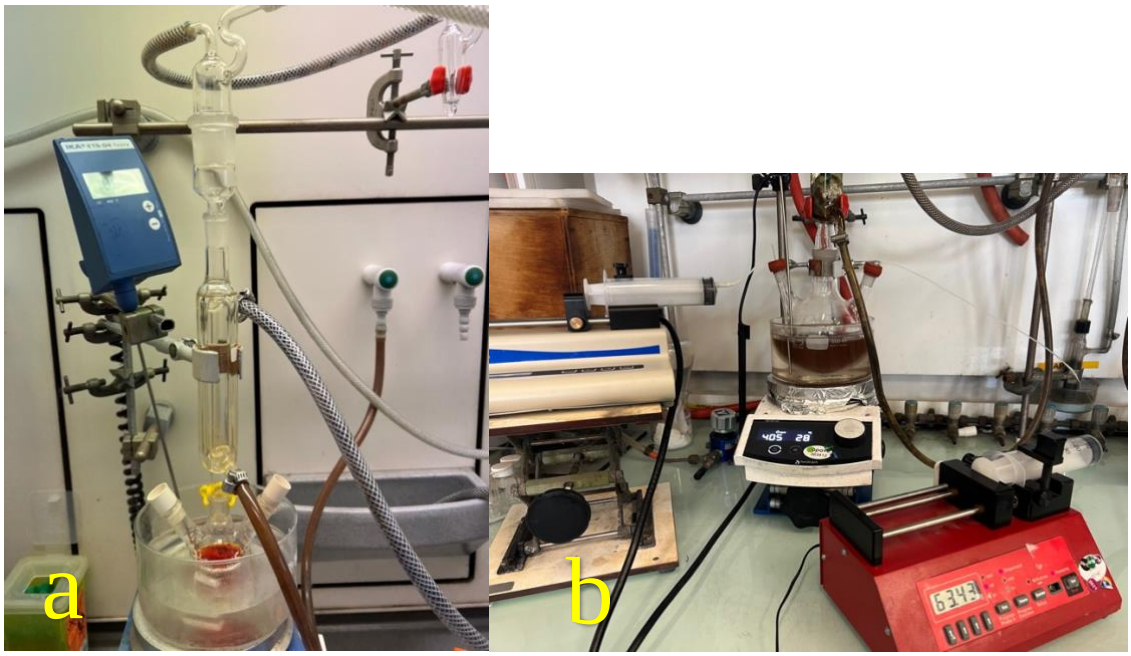

Figure 2. The apparatuses used to synthesise quantum dot nanoparticles (a) and gold nanoparticles (b).

2.1.1. Ultraviolet-visible spectrometry and fluorescence spectroscopy

During the synthesis of quantum dots, multiple samples were taken from the reaction flask to analyse the progress and end of the reaction based on the absorbance and the location of the fluorescence maximum of the product. Measurements were done using ultraviolet-visible (UV-VIS) spectrometry and spectrofluorometry.

Sample (< 0.5 mL) was taken from reaction flask and diluted with Milli-Q water in an approximate volume due to undiluted sample generally having too intense photoluminescence for measurements. In addition, dilution is preferred due to the linearity of photoluminescence's and absorbance's relation to concentration decreasing as the concentration increases. First, the absorbance of the sample was measured using the diode-array UV-VIS spectrometer, and the photoluminescence of the sample was measured subsequently.

The absorbance of the sample at 400 nm was used to normalise the photoluminescence of different samples of the same synthesis with different concentrations. The normalisation was based on the sample with the highest absorbance, whose photoluminescence data was not normalised. The photoluminescence of other samples was divided by the fraction of the sample's absorbance at 400 nm of the absorbance of the sample with the highest absorbance.
The samples were measured in a 4×10 mm quartz cuvette. The UV-VIS spectrometer used was Hewlett Packard 8452A single beam diode array UV-vis spectrophotometer with a range from 190 to 820 nm, a resolution of 2 nm, and equipped with deuterium discharge lamp. The utilised fluorescence spectrophotometer was Hitachi F-4500 equipped with a 150 W Xenon lamp and a R3788 photomultiplier tube detector. The excitation wavelength was set at 400 nm, and photoluminescence was measured from 420 nm to 900 nm with a scan speed of 1200 nm min^{-1}. The excitation slit width was 10 nm, and the emission slit width was 5 nm.

2.1.2. Synthesis of quantum dots and nanoparticles

CuInZnS quantum dots synthesis

The synthesis of CuInZnS (CIZS) quantum dots was based on the procedure done by Xu et al. [45], and the list of reagents and synthesis conditions is specified in **Table 1**.

Table 1. The reagents and their quantities used in CuInZnS quantum dots synthesis. Solubilisation specifies the medium used to solubilise the solid reagents before inserting them to the reaction flask.

Chemical	L-Glutathione	$InCl_3$	$CuCl_2 \times H_2O$	$Zn(OAc)_2 \times 2H_2O$	Na_2S
Molar equivalent	10	9	1	1	10
Molar mass (g mol^{-1})	307.32	221.18	170.48	219.50	240.18 (nonahydrate)
Measured mass (mg)	307.45	198.6	17.13	21.04	243.3
Solubilisation	2 mL H_2O + 50 µL M NH_4OH + 5 min sonication	1 mL 0.25 N HNO_3	1.5 mL H_2O	1.5 mL H_2O	2 mL H_2O

L-gluthathione (GSH) solution was inserted into the reaction flask, followed by $InCl_3$ solution and 2 mL of water. Next, 1.5 mL of 5 N NH_4OH was added to regulate the pH to around 9. Subsequently, zinc acetate was added, followed by copper chloride. For a brief moment, a black precipitate formed, which dissolved immediately. 2 M citric acid was added until the pH was around 7. Finally, sodium sulphide solution was added rapidly, and the solution coloured yellow. The reaction mixture was heated to 100 °C, and the reaction continued at elevated temperatures for 150 minutes. The sample was taken from the reagent flask every 30 minutes, starting at the reaction mixture reaching 100 °C. After 30 minutes, the solution turned red, and the colour intensified throughout the reaction. After 150 minutes, the heating was ceased, and solution allowed to reach room temperature. After purification, the collected 166.2 mg of quantum dots were solubilised in 3 mL of water to stabilise them and avoid degradation while in storage.

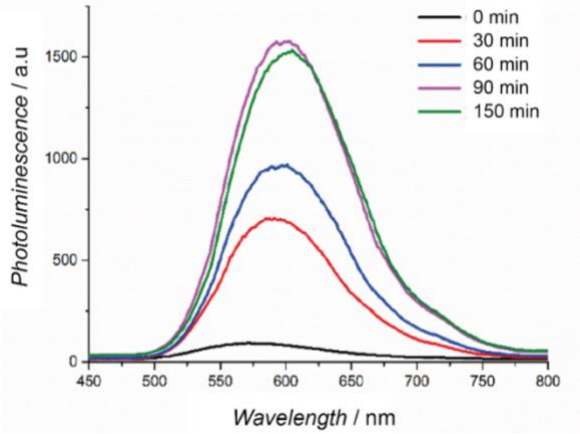

Figure 3. Measured photoluminescence of CuInZnS quantum dots synthesis solution at different times of the ongoing reaction. The photoluminescence emission maximum of the product (150 min) was at 605 nm.

The exact molecular formula for the expected 1:1 Zn:Cu ratio is $Cu_{0.270}In_{1.463}Zn_{0.202}S_2$ [45]. However, the normalised photoluminescence maximum at 605 nm (**Figure 3**) refers to 15:1 Zn:Cu ratio with the formula $Cu_{0.199}In_{1.046}Zn_{0.833}S_2$ [45].

$CuInS_2$ quantum dots synthesis

The synthesis of $CuInS_2$ (CIS) quantum dots was based on a procedure done by Chen et al. [46], and the list of reagents is specified in **Table 2**.

Table 2. The reagents and their quantities used in $CuInS_2$ quantum dots synthesis. Solubilisation specifies the medium used to solubilise the solid reagents before inserting them to the reaction flask.

Chemical	GSH	$InCl_3$	$CuNO_3 \times 3\ H_2O$	Na_2S
Molar equivalent	5	4	1	5
Molar mass (g mol^{-1})	307.32	221.18	241.6	240.18 (nonahydrate)
Measured mass (mg)	308.70	178.10	48.71	242.03
Solubilisation	2 mL H_2O + 50 µL 5 M NH_4OH + 5 min sonication	1 mL 0.25 M HNO_3 + 2 mL H_2O	2 mL H_2O	2 mL H_2O

The GSH solution was inserted into the reaction flask, followed by the $InCl_3$ solution. Next, 1.7 mL of 5 N NH_4OH was added to regulate the pH to around 9.5. Subsequently, copper nitrate solution was added which created quickly disappearing black precipitate. 2 M citric acid was added until pH was around 6.5 (1.2 mL was required). Finally, sodium sulphide solution was added rapidly, and the solution coloured yellow. The reaction mixture was heated to 100 °C, and the reaction continued at elevated temperatures for 60 minutes (**Figure 4**). Beginning at the reaction mixture reaching 100 °C, the sample was taken from the reagent flask every 15 minutes. The solution turned red after 15 minutes, and the colour reached intense dark red after 45 minutes. No colour change was noted later. After 60 minutes, the heating was ceased, and solution allowed to reach room temperature. After purification, the collected 824 mg of quantum dots were dispersed in 8 mL of water to stabilise them and avoid degradation while in storage. The size of the quantum dots was 18 (±5) nm according to analysis of scanning electron microscopy (SEM) pictures (**Figure S3.1, in Supplementary 3**)

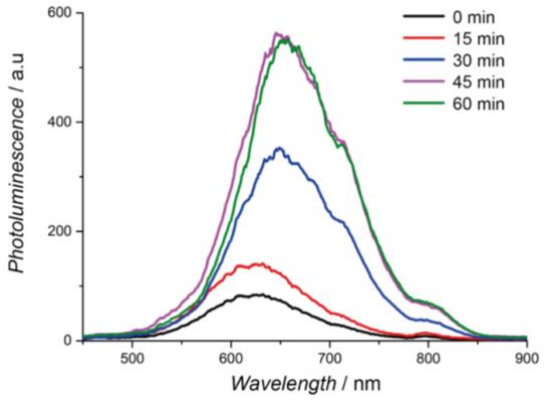

Figure 4. Measured photoluminescence of $CuInS_2$ quantum dots synthesis solution at different times of the ongoing reaction. The photoluminescence emission maximum of the product (60 min) was at 657 nm.

AgInS:Cu quantum dots synthesis

Silver-Indium-sulphur quantum dots doped with copper were synthesised as follows (**Table 3**).

Table 3.The reagents and their quantities used in AgInS:Cu quantum dots synthesis. Solubilisation specifies the medium used to solubilise the solid reagents before inserting them to the reaction flask.

Chemical	GSH	$InCl_3$	$AgNO_3$	$Cu(NO_3)_2 \times 3\ H_2O$	Na_2S
Molar equivalent	60	40	10	1	50
Molar mass (g mol^{-1})	307.32	221.18	170.48	219.50	240.18 (nonahydrate)
Measured mass (mg)	369.54	178.01	34.03	4.81	240.51
Solubilisation	4.9 mL H_2O + 50 µl 5 M NH_4OH	2 mL 0.5 M HNO_3 + 2.5 mL H_2O	1 mL H_2O	0.2 mL H_2O	2 mL H_2O

The GSH solubilisation required 5 minutes of sonication in an ultrasonic bath. The solution was transferred to the reaction flask, followed by the $InCl_3$ solution. Next, 1.3 mL of 5 M NH_4OH was added to regulate the pH to around 9. A white precipitate appeared, which disappeared after a few seconds. Subsequently, silver nitrate and copper nitrate solutions were added. 2 M citric acid was added until the pH was around 7. Finally, sodium sulphide solution was added rapidly. The reaction mixture was heated to 100 °C, and the reaction continued at elevated temperatures for 60 minutes (**Figure 5**). After the mixture reached 100 °C, the sample was taken from the reagent flask every 15 minutes. Following purification, the collected 453.7 mg of quantum dots were solubilised in 5 mL of water to stabilise them and avoid degradation while in storage.

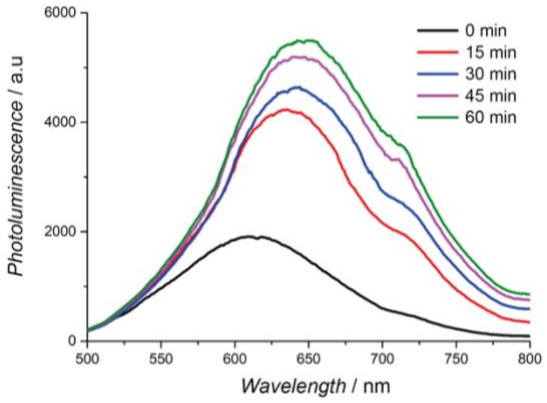

Figure 5. Measured photoluminescence of AgInS:Cu quantum dots synthesis solution at different times of the ongoing reaction. The photoluminescence emission maximum of the product (60 min) was at 650 nm.

Cu_2S quantum dots synthesis

The synthesis of Cu_2S quantum dots was based on the procedure done by Yue et al. [47], and the list of reagents is specified in **Table 4**.

Table 4. The reagents and their quantities used in Cu_2S quantum dots synthesis. Solubilisation specifies the medium used to solubilise the solid reagents before inserting them to the reaction flask.

Chemical	Thioglycolic acid	CuBr	Na_2S
Molar equivalent	8	4	1
Molar mass (g mol^{-1})	92.12	143	240.18
Mass (mg)	184.24	143	59.55
Measured mass (mg)		99.47	61.02
Measured volume (µl)	148		
Solubilisation			3 mL H_2O

First, 100 mL of water was heated to 90 °C. The solution was stirred for 30 min to clear the oxygen from the synthesis apparatus. Thioglycolic acid was added and stirring continued for 10 minutes. Copper bromide powder was added, resulting in the solution turning yellow. The pH was measured to be about 5 and stirring continued for 45 minutes. Next, pH was regulated to about 10 by adding 5.5 mL of 1 N NaOH solution. The solution became clear and transparent, and stirring continued for 5 minutes. Finally, sodium sulphide was added, and the solution turned brown. Stirring was continued for 15 min, and the colour intensified during the first minutes of stirring. The heat was removed, and the solution was allowed to cool down overnight. After mixing the product with ethanol and purification at 3500 rpm, the collected

130 mg of quantum dots were dispersed in 5 mL of water to preserve them and avoid degradation while in storage.

Synthesis of 55 nm gold nanoparticles

The aim was to synthesise 80 nm AuNPs following the Ziegler and Eychmüller method [48], for which the precursors were 12-nanometer AuNPs, synthesised by the Turkevich method [49]. A three-necked 500 mL reaction flash was cleaned thoroughly with ethanol and in-house prepared aqua regia to eliminate any potential agglomeration points and installed with a vertical condenser and magnetic stirrer. 0.294 mmol of $HAuCl_4 \times x\ H_2O$ (weighed 97 mg based on anhydrous mass) and 1.59 mmol of sodium citrate (weighed 467 mg) were separately solubilised in 50 mL of water. Gold (III) chloride solution was inserted into the reaction flask and brought to a boil in an oil bath. Sodium citrate solution was added rapidly, and the initial yellow solution turned transparent. After two minutes of boiling, the solution began quickly darkening, and after three minutes, the solution had obtained a dark red colour, which was to be expected [49,50]. In total, solution boiled for 8 minutes and was then allowed to cool down. The solution was stored at 4 °C in a dry and clean bottle. Solution volume was measured, and assuming the gold precursor reacted entirely, the product concentration was 191.9 mg/L. Using SEM-imaging, the size of the gold nanoparticles was confirmed to be 12 (±1) nm (**Figure S3.3a**).

Similarly, the 80-nanometer AuNPs were synthesised using the same reaction flask cleaned with aqua regia following Ziegler and Eychmüller method [48], and the basis for synthesis was 12-nanometer AuNPs seed solution (120 mL, 11.5 mg/L). The reactant solution in the first syringe was 170.8 mg $HAuCl_4 \times H_2O$ (weighed 176.2 mg based on anhydrous mass) solubilised in 60 mL of water, and the solution in the second syringe was 246 mg of sodium citrate dihydrate mixed with 126 mg of ascorbic acid and solubilised in 60 mL of water. In 45 minutes, both reactant solutions were added to the seed solution in the flask at 1.33 mL/min using syringe pumps (Fischer Scientific and WPI BS-8000). Then, the flask was heated to 92 °C, remained at an elevated temperature for one hour, and was finally allowed to cool down. The colour change was from light red to dark red to purple to hazy brownish-red. Product concentration was 238.5 mg/L, assuming the precursor reacted entirely. However, the SEM imaging proved the AuNPs to be smaller than expected 55 (±8) nm (**Figure S3.2**).

2.2. Synthesis of silicon nanowires

The silicon nanowires were grown on a porous carbon structure. Dispersed nanoparticles were deposited on the carbon samples and acted as the seeds for the growth of silicon nanowires. The growth took place in a homemade reactor at high temperature and pressure together with diphenylsilane acting as silicon source for the growth. After growth, the samples were cleaned of diphenylsilane and by-products, and taken to electrochemical procedures to further modify the surface of the cathode and assess the activity of the material when working as the photoelectrochemical cathode.

2.2.1. Sample preparation

The silicon nanowires were grown on commercial carbon-based gas diffusion layer (GDL) used in hydrogen fuel cells (Sigracet 39 AA, FuelCellStore). The carbon support acts as the perfect substrate for photoelectrochemical cathode, providing good electrical conductivity and allowing hydrogen bubbles to easily escape the cathode surface. The GDL samples were cut as 2.54 × 0.635 cm pieces and marked with small cut-outs at the top to differentiate samples.

Drop-casting on a hot plate (120 °C) was used to deposit nanoparticles on the GDL substrate. The hot plate surface was covered with aluminium foil, the actual temperature was most likely lower. Since GDL is very hydrophobic and the primarily used colloidal nanoparticles — quantum dots — were stored in water, the particles could not be drop-cast directly on the GDL. Hence, acetonitrile was used. Wetting the GDL with smaller and greater volumes before drop-casting aqueous nanoparticles was attempted, however pre-mixing water and acetonitrile before drop-casting proved to be more effective. The ratio of water and acetonitrile largely dictates the rate of nanoparticles' diffusion in and on GDL. The goal was to have homogeneous spread of nanoparticles on the surface and decreasing gradient of nanoparticles from surface towards opposite side of GDL. Greater proportion of acetonitrile promotes faster wetting and distribution, and greater proportion of water helps not diffuse too deep into GDL. Different volumetric ratios from 1:4 to 4:1 were experimented and acetonitrile to water ratio 0.9:1 was concluded as the best option. AuNPs were redispersed in anhydrous ethanol. Synthesis solution was centrifugated at 6000 rpm for 5 minutes, the supernatant was removed, and enough ethanol added to have desired concentration. Even though the supernatant was not completely transparent, SEM imaging proved that the average size of AuNPs did not change before and after centrifugation.

Another important factor is the deposited volume. It was discovered that samples dry faster on the edges, therefore depositing too large volume creates a small-scale solution flow from

middle of the sample to the outer areas and hence, also flow of nanoparticles. However, too small volume is not enough to cover the whole surface of the sample. The final volume settled for was 80 µl. The deposition volume and acetonitrile to water ratio were chosen on a visual observation of wetting and the observation of grown silicon nanowires using different deposition parameters.

2.2.2. Silicon nanowires synthesis and cleaning

The growth of silicon nanowires took place in a 70 cm^3 or a 175 cm^3 stainless-steel reactor equipped with thermocouple, pressure sensor, and relief valve with a 25-bar limiter. Each growth is described as a synthesis batch or simply batch. For one synthesis batch, 6 mL or 15 mL of diphenylsilane was used in a smaller or bigger reactor, respectively, and 18 to 24 GDL samples, were used in the reactor. The samples were placed in the reactor with crucibles covered with stainless steel lid to avoid diphenylsilane condensation dripping into the crucibles. The reactor was degassed three times and filled with argon in between degassing. The reactor was heated to 430 °C in 30 minutes, remained at elevated temperature for 3-4 hours, and was finally left to cool down to room temperature. While heating, the pressure inside the reactor reached up to 16 bars. After reaching room temperature and releasing excess pressure from the reactor, the samples were cleaned of the by-products with acetone and dichloromethane and dried on a hot plate at 40 °C. A total of 6 synthesis batches were completed. The exact set of samples and used nanoparticles is specified in Supplementary 4.

2.2.3. Silicon nanowire synthesis yield

The samples were weighed before and after nanoparticles deposition, and after SiNW growth using Metller Toledo AE260S and Sartorius MC 210 S scales. These measurements were used to determine the weight of the deposited nanoparticles and the grown SiNWs. The yield (the ratio of grown silicon weight to used nanoparticle weight) was calculated to estimate the speed of the SiNWs growth from the specific nanoparticle seed. Separate tests determined that the carbon gas diffusion layer lost 13% of its mass during SiNW synthesis heating program. This loss was taken into account when calculating the mass of SiNWs. However, mass loss due to decomposition of nanoparticle core and ligands was not taken into account.

2.3. Electrochemical measurements

SP-300 Bio-Logic or VSP-300 Bio-Logic potentiostats were used for catalyst electrodeposition and photoelectric current measurements of the samples. All methods were run in a three-electrode system, where the photocathode sample acted as the working electrode, platinum wire

as the counter electrode, and in-house-made Ag/AgCl electrode in 3 M KCl solution as the reference electrode.

Prior to each series of electrochemical procedures, the potential of the reference electrode against SHE (standard hydrogen electrode) was verified using cyclic voltammetry (100 mV s^{-1}, 0.4 to −1.2 V) in a pH 7 phosphate buffer solution containing potassium hexacyanoferrate(III) (Sigma Aldrich, ≥ 98.0%). The working electrode was polished glassy carbon and the counter electrode was platinum. The formal reduction potential of iron(II/III)-complex against the Ag/AgCl/3 M KCl electrode in phosphate buffer was determined by averaging the anodic and cathodic peak potentials of the cyclic voltammograms. The actual potential of the Ag/AgCl/3 M KCl against SHE can be calculated by subtracting the formal potential of the iron(II/III)-complex against the Ag/AgCl/3 M KCl electrode from the standard potential of iron(II/III)-complex against SHE in phosphate buffer [51]. This enables the conversion of measured potentials from the Ag/AgCl/3 M KCl reference electrode scale to the SHE scale. Two separate Ag/AgCl reference electrodes were used for photocurrent measurements and electrodeposition of the catalyst to avoid cross-contamination.

2.3.1. Photoelectric current measurements

The photoelectrochemical measurements were conducted in 0.5 M H_2SO_4 solution (expected pH 0.3) in a purpose-designed cell with a quartz-window. The solution was saturated by bubbling with nitrogen gas before and during the measurements to remove oxygen from the system. Xenon lamp (280 W) equipped with an air mass 1.5G filter, commonly used for photocurrent measurements [3,27,32], simulated the natural sunlight during measurements (100 mW cm^{-2}).

Photoelectric current was measured by performing linear sweep voltammetry (LSV) from 0.2 V to −0.5 V vs SHE at 10 mV/s or at 5 mV/s to increase the resolution when necessary. First, for each series of samples a set amount of stabilising LSV cycles were performed in dark and light conditions to confirm the stability of the sample. Then, LSV was performed in fluctuating light condition, where light was repeatedly turned on and off with a lamp shutter. Photoelectric current was measured from the fluctuating light graph as the average of current differences of two closest light to dark and dark to light transitions closest to the desired potential −0.15 vs SHE. Graphical explanation can be found in Supplementary 5.

2.3.2. Catalyst deposition

Amorphous MoS_x catalyst has been shown to be excellent catalyst for photocathodes [5,31] and was thus used in this work. MoS_x catalyst was deposited on the SiNW samples using three different methods: drop-casting, spray-coating, and electrodeposition.

Solution of 1 mg of catalyst MoS_x powder, 160 µl of ethanol, 40 µl of MilliQ water and 10 µl of 5% Nafion solution (Sigma Aldrich, Nafion 1100W) was prepared for drop-casting and spray coating. Argon flow with relative backpressure of 1 bar was used to spray-coat the samples from a distance of 7 cm. Due to wide spray cone, some of the sprayed ink did not land on the sample and the final ink loading of the sample is unknown. Single spray-cast volume was 200 µL and single drop-cast volume was 50 µL. Drop-casting was completed with an automatic pipette. The samples were dried at least 30 minutes before applying subsequent amount of catalyst suspension.

Electrodeposition of MoS_x on the silicon nanowires was done in electrodeposition bath of $[MoS_4](NH_4)_2$ (Sigma Aldrich, 99.97%) in pH 7 phosphate buffer. The counter and reference electrode were the same as in previous methods. Depositing potential was set at 0.1 V vs SHE and the total amount of charge passing by the active area of the electrode was 9 mC cm^{-2}. After deposition, the sample was washed with water and ethanol.

2.4. Physical characterisation

ZEISS Ultra55A Scanning electron microscope with energy dispersive X-ray (SEM-EDX) XFlash 5030 sensor and FEG-Shottky electron source was used to observe and characterise synthesised nanoparticles and SiNWs. SEM images provided information about the shape of the nanowires grown using different nanoparticle seeds. Subsequently, ImageJ software was used to measure the widths of the nanowires from SEM images.

2.5. Artificial intelligence

Microsoft Copilot artificial intelligence chatbot was used to verify the spelling and grammar of selected paragraphs of this work. The use of Microsoft Copilot is in accordance with University of Tartu guidelines for using artificial intelligence chatbots for teaching and studies.

3. Results

3.1. Silicon nanowire growth

3.1.1. Morphology of the silicon nanowires

The characteristic images of investigated silicon nanowires can be found in supplementary 6. The morphological descriptions, widths, and growth yields of SiNWs can be found in **Table 5**. The best replacement for Au-grown SiNWs are CIS-grown SiNWs due to close resemblance in shape, high yield and good growth rate compared to other nanoparticle seeds (**Table 5**, **Figure 6**). There is no difference in yield of CIS and CIZS nanoparticles grown in the same synthesis batch (synthesis 1 and 2). However, is CIS is used in the same synthesis batch with Au nanoparticles, the yield of CIS-grown SiWNs decreases (synthesis 4), indicating the preference of silane decomposition on nanoparticles.

Table 5. Summary of the morphological descriptions, widths of the silicon nanowires at different nanoparticle loadings on the sample, and growth yields of silicon nanowires grown from different nanoparticles. (*) the notation indicates a sample series that had no SiNWs detectable by the human eye.

Nano-particle	Morphological description	Silicon nanowire width at different nanoparticle loadings	Yield (Silicon to nanoparticle weight ratio)
CIS	Slightly curved, narrow, homogeneous, and with a wide distribution of diameters. Microscale spider-web like structures are present.	13 (±11) to 36 (±12) nm at 12 to 105 μg cm^{-2}	Batch 1: 50 (±33) Batch 2: 29 (±5) Batch 3: 28 (±6) Batch 4: 21 (±12) Average: 32 (±19)
CIZS	Slightly curved, narrow, homogeneous, and with a wide distribution of diameters. Microscale spider-web like structures are present.	12 (±4) to 42 (±17) at 2 to 56 μg cm^{-2}	Batch 1: 53 (±24) Batch 2: 34 (±5)
ZnS	No SiNWs could be grown	-	-
AgS	No SiNWs could be grown	-	-
CuS	Straight and large in diameter.	48 (±24) at 68 μg cm^{-2}	Batch 5: 33 (±29
CuS (degraded)	Straight nanowires emerge from hotspots like bushes.	53 (±20) to 63 (± 31) at 63 to 310 μg cm^{-2}	Batch 6: 10 (±8)
In_2S_3	Wide and very twisted.	83 (±18) to 55 (±31) nm at 310 to 1860 μg cm^{-2}	Batch 5: 1 (±0) Batch 6: 1 (±1)
CuZnS	Minor growth in the form of small bushes across the sample.	51 (± 29) nm at 68 μg cm^{-2}	Batch 5: 44 (±24) *
AgSnS	Long and wide SiNWs with bushes at the tips of SiNWs and on the surface of carbon fibres.	58 (±22) to 198 (±63) nm from 62 to 496 μg cm^{-2}	Batch 6: 12 (±11)*
AgSnZnS	A mixture of long wide nanowires with visible nanoparticles at the tips and short coiled nanowires at the surface of the carbon fibres.	36 (±14) to 73 (±53) nm from 62 to 558 μg cm^{-2}	Batch 6: 12 (±9)*
CuSnS	Straight wires with twisted deformities at the tips of the wires. SiNW hotspots present.	56 (±22) to 67 (±32) nm at 62 to 558 μg cm^{-2}	Batch 6: 6 (±5)
SnInS	Large and variously deformed; SiNWs cover the carbon fibres densely and do not extrude.	98 (±61) nm at 558 μg cm^{-2}	Batch 6: 17 (±17)*
AgInS:Cu	Twisted similarly to In_2S_3-based SiNWs but the wires are smaller and have less deformities. Poor coverage of SiNWs on carbon fibres	37 (±17) to 61 (±31) nm at 62 to 558 μg cm^{-2}	Batch 6: 16 (±13)*
Au	Slightly curved, homogeneous, low deformities [3]	Not measured	Batch 4: 29 (±12)

In_2S_3 required significantly higher nanoparticle loading compared to other nanoparticles for sufficient growth. Although SiNWs were detectable by SEM also at low loadings, no SiNWs could be observed at low loading visually by eye. For AgSnS-grown SiNWs, it should be noted that sometimes a spherical nanoparticle replaces the bush at the tip of SiNW. Qualitative SEM-EDX analysis of the nanoparticle detected Cu instead of Ag and Sn which might be caused by contamination.

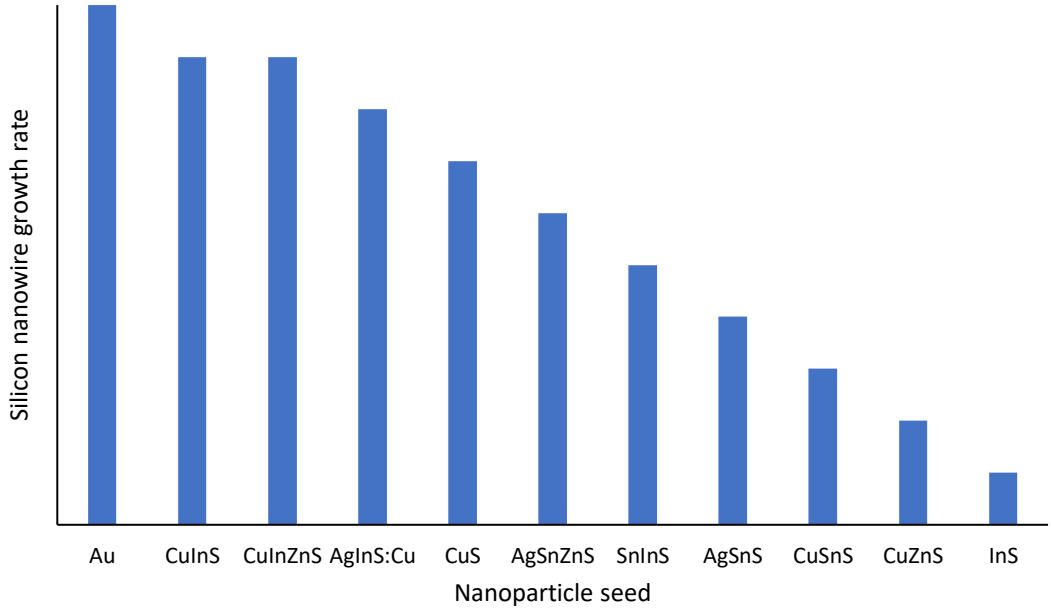

Figure 6. Qualitative estimation of silicon nanowire growth rates of used seeds based on silicon to nanoparticle weight ratio of the growths and the visual comparison of samples within one synthesis batch and across different synthesis batches.

3.1.2. Silicon nanowire diameter as a function of nanoparticle concentration

Due to higher surface atoms to bulk atoms ratio, and the higher energy of surface atoms, the melting temperature of nanoparticles is reduced compared to bulk material. During heating of the reactor, some of the nanoparticles may merge, creating bigger nanoparticles. Higher concentration of deposited nanoparticles results in more merging, bigger nanoparticles and wider SiNWs. This is illustrated well by the general trend of SiNW diameter increasing with nanoparticle concentration, In_2S_3-based SiNWs being the only exception. In addition, separate SiNW diameter measurement was completed on the surface and inside of a 50 μg cm^{-2} CIS-based SiNW sample after cutting the sample in half. The average diameter of SiNWs were 36 (±35) nm and 20 (±18) nm in the surface and inside the the sample respectively.

To confirm the hypothesis of nanoparticles merging during heating, 12 nm AuNPs, measured size 12 (±1) nm, were deposited on the carbon support and heated in the presence of argon using the same heating program as for the synthesis of SiNWs. After heating, the nanoparticles were grown in size to 39 (±20) nm. Increased standard deviation indicates that

the exact size of increased nanoparticles depends on the specific concentration of the nanoparticles in the local region. However, it's important to note that the heating of the nanoparticles took place under atmospheric pressure, in contrast to the synthesis of SiNW, during which the pressure was increased to 16 bars.

3.2. Photocurrents of photocathodes

CIS-based SiNWs were chosen to replace Au nanoparticles on the photocathode due to straight and homogeneous SiNWs like Au-grown SiNWs, stability of the nanoparticles' colloidal solution and high silicon to nanoparticles ratio during the growth. In addition, CIZS, $In_2S_3$and CuS-based SiNWs were also compared.

3.2.1. Photocurrent of $CuInS_2$-based photocathode without catalyst

When compared to AuNP-based photocathode, CIS-based photocathode in the same series exhibited a lower photocurrent (**Figure 7**). The peak of CIS-based photocathode was 4.4 µA cm^{-2}, maxing out around 62 µg cm^{-2}, AuNP-based photocathode reached 9.6 µA cm^{-2} at 87 µg cm^{-2}.

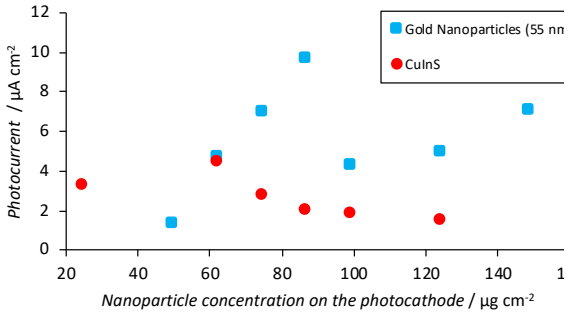

Figure 7. Dependence of photocurrent on nanoparticle concentration for photocathodes with silicon nanowires based on $CuInS_2$ nanoparticles (Batch 4) and gold nanoparticles.

However, the consistency of the photocurrent of CIS-based photocathodes across series was poor (**Figure 8**). Batch 2 showed significantly higher photocurrents at 50-62 µg cm^{-2} than other batches despite being synthesised using the same amount of nanoparticles. The higher current of batch 2 can most likely be attributed to the visually denser coverage of SiNWs on the photocathode (**Figure S7**). Even so, the maximum photocurrent resides around 60 µg cm^{-2}.

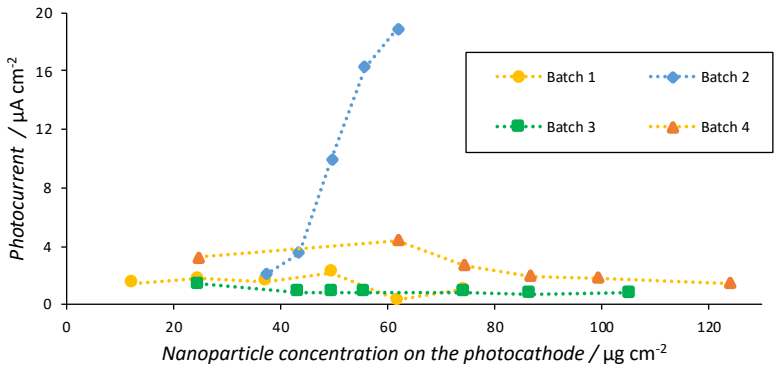

Figure 8. Dependence of photocurrent on nanoparticle concentration for photocathodes from batches 1–4 with silicon nanowires based on $CuInS_2$ nanoparticles.

3.2.2. The effect of catalyst on photocurrent

Electrodepositing the MoS_x catalyst on the photocathode has a strong positive impact on the photocurrent. The maximum photocurrent of CIS-based photocathodes increased up to 16 times within a series (**Figure 9**). Albeit the increase in photocurrent was high, the CIS-based photocathodes failed to surpass the performance of AuNP-based photocathodes, which might be due to the baseline photocurrent of AuNP-based photocathode without catalyst being higher than that of CIS-based photocathode to begin with. The AuNP-based photocathode reached 34 µA cm^{-2} at 100 µg $cm^{-2,}$ while the CIS-based photocathode reached 16 µA cm^{-2} at 74 µg cm^{-2} (**Figure 9**). However, the results are well below the 250 µA cm^{-2} reported in the literature originating from a photocathode with SiNWs based on 48 nm AuNP and coated with molybdenum sulphide catalyst [3].

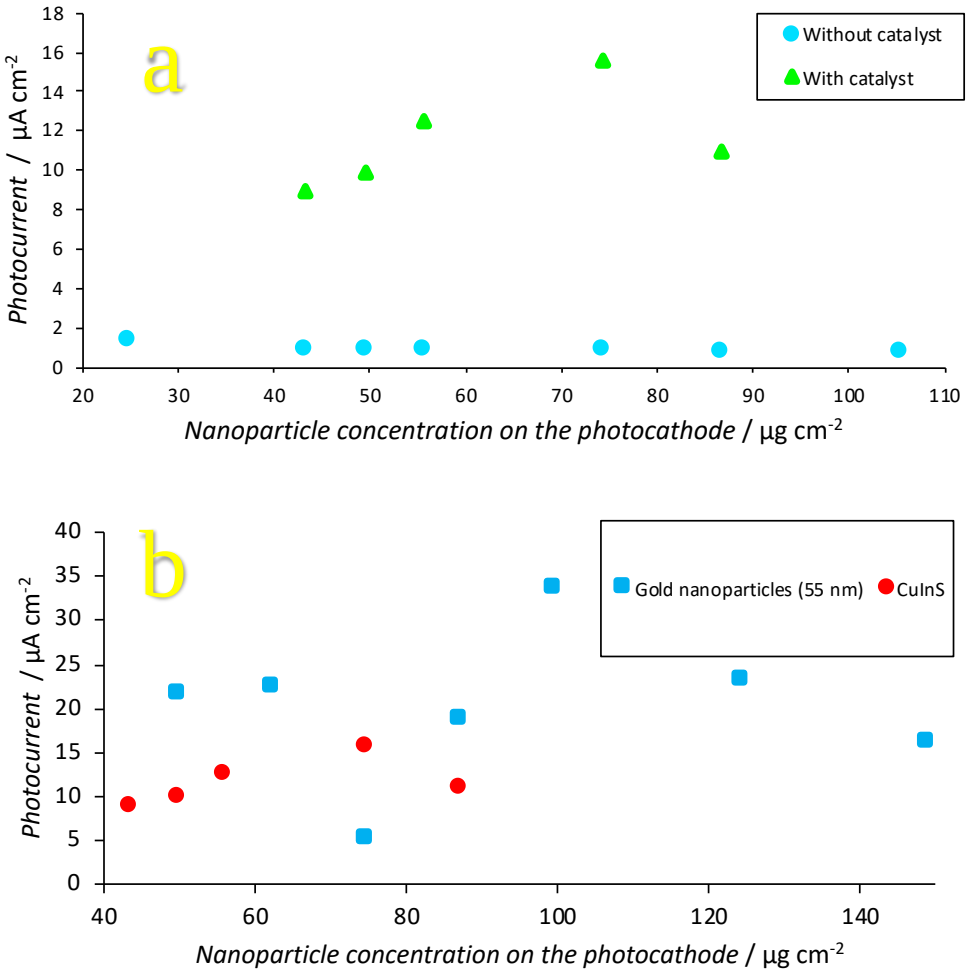

Figure 9. Dependence of photocurrent on nanoparticle concentration for photocathodes with silicon nanowires based on $CuInS_2$ nanoparticles with and without coating with MoS_x catalyst (a), and dependence of photocurrent on nanoparticle concentration for photocathodes with silicon nanowires based on $CuInS_2$ (CIS) and Au nanoparticles and covered with MoS_x catalyst (b)

Spray-coating and drop-casting compared with electrodepositing. Not all catalyst deposition methods are created equal. The drop-casting and spray-coating methods provided much smaller gains in photocurrent compared to electrodepositing. The baseline photocurrent without catalyst coating was 0.86 µA cm^{-2} (at 56 µg cm^{-2}), drop-casting 100 µL of catalyst suspension increased the photocurrent to 4.2 (±0.3) µA cm^{-2} and spray-coating 400 µL of suspension increased the photocurrent to 3.6 (±2.0) µA cm^{-2}. What's more, increasing or decreasing the amount of catalyst suspension showed no clear trend in the change of photocurrent. The photocurrent increase is small compared to 15 µA cm^{-2} reached with electrodeposition method at the same nanoparticle density. Observing the drop-cast and spray-coated photocathode in SEM revealed that the catalyst suspension formed big agglomerates rather than a uniform coating on the nanowires (**Figure 10**). The agglomerates have smaller electrochemically active area compared to uniform coating and poor electrical contact with the nanowires. Therefore, the catalytic effect is inferior compared to electrodeposition method.

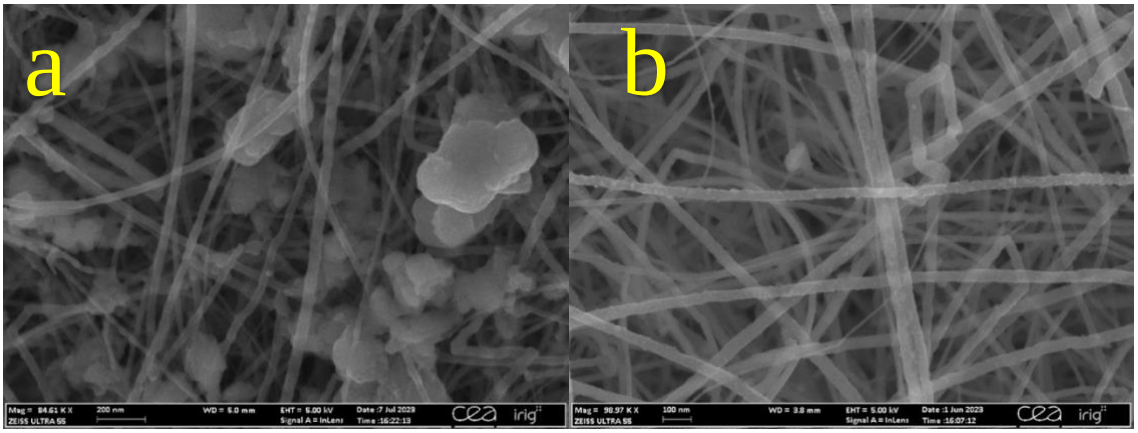

Figure 10. Scanning electron microscope images of silicon nanowire photocathode. MoS_x catalyst suspension has been deposited on the photocathode using spray-coating technique (a), which created undesired agglomerates, and electrodeposition technique (b), which applies a uniform coating. Silicon nanowires were grown on a porous carbon gas diffusion layer.

3.2.3. Photocurrent of CuInZnS-based photocathode

When compared to the CIS-based silicon nanowire photocathodes, the CIZS nanoparticles-based silicon nanowire photocathode performed very similarly (**Figure 11**). The minor deviation in photocurrent is likely caused by the repeatability of the electrode preparation. Coupled with the findings from SiNW growth using ZnS seeds, one can state that zinc has no effect on the growth of nanowires and does not affect electrochemical behaviour.

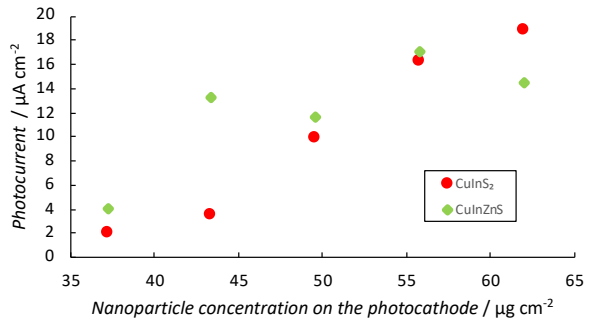

Figure 11. Dependence of photocurrent on nanoparticle concentration for photocathodes with silicon nanowires grown from $CuInS_2$ and CuInZnS nanoparticles.

3.2.4. Photocurrents of CuS and In_2S_3-based photocathodes

Due to large diameter of the nanowires and extreme shapes of the nanowires, CuS- and In_2S_3-based photocathodes were also investigated. However, both produced poor results (**Figure 12**). The straight shape of CuS SiNWs and twisted shape of In_2S_3 SiNWs has no good effect on the photocurrent of the photocathode. Moreover, since both nanoparticles require large concentrations for SiNW synthesis, especially In_2S_3, they are inferior to CIS nanoparticles.

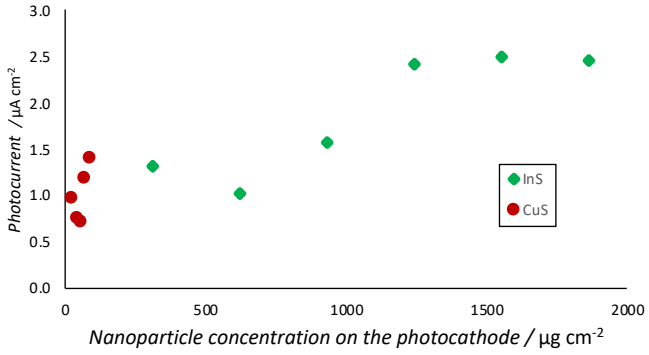

Figure 12. Dependence of photocurrent on nanoparticle concentration for photocathodes with silicon nanowire grown from CuS and InS nanoparticles.

3.2.5. Cycling effect

While investigating the long-term photocurrent of a photocathode with SiNWs grown from CIZS nanoparticles (62 µg cm^{-2}), 90 minutes of linear sweep voltammetry cycles increased from the photocurrent 4 to 57 µA cm^{-2} which was highest recorded photocurrent on any sample. SEM examination of the photocathode revealed small white dots on the nanowires (**Figure 13**) which are not apparent other uncycled samples.

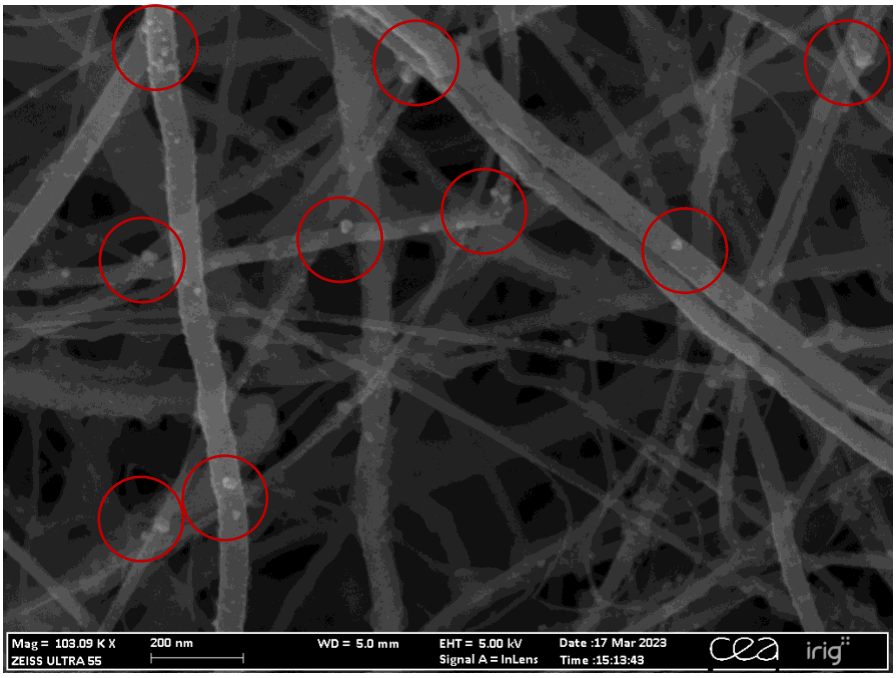

Figure 13. Silicon nanowires grown from CuInZnS nanoparticles after 90 minutes of linear sweep voltammetry cycles. Silicon nanowires were grown on a porous carbon gas diffusion layer.

4. Discussion

Shape of Silicon nanowires. Combining various metals in nanoparticles has produced evidence of each metal's influence on the shape of the nanowires. As seen with monometallic sulphides, copper produces straight, rigid and thick nanowires, and indium grows wide and extremely twisted nanowires. However, their combination, CIS nanoparticles, produces narrow nanowires whose shape is a combination of earlier two: straight and slightly bendy. Since CIZS-based nanowires have morphology identical to CIS-based nanowires and ZnS nanoparticles produced no detectable SiNWs, it seems that zinc has no visible effect on the formation of crystalline silicon and ZnS is too stable to decompose in the reactor. Using Ag in nanoparticles leads to formation of nanowire bushes either at the surface of carbon fibres, as seen with AgSnS nanoparticles, or at the tips of nanowires, as seen with AgSnZnS nanoparticles. In addition, the bush-like structures dominated in AgInS:Cu-grown SiNWs along with twisted nanowires originating from the influence of In. Copper doping has little effect, although the presence of some straight nanowires can be attributed to copper. AgSnZnS, AgSnS demonstrate that Sn is creating long and discrete nanowires, although in the case of CuSnS nanowires, the influence of Sn is not apparent and the cause of minor deformations alongside straight wires is unknown. SnInS-based SiNWs also show straight and discrete influence of Sn but is combined with twisted shape originating from In. The results differ from the reports of successful SiNW synthesis with Zn and Ag metals [4]. The difference may be either due to different chemical stability of sulphide compared to pure metal such as different melting point, or the unsuccessful synthesis of the seeds.

However, no composition analysis was performed for the seeds to confirm the expected composition. The actual composition may deviate from the theoretical composition and the impurities may be present, altering the results of the analysis. For further analysis, the elemental composition could be measured with inductively coupled plasma mass spectrometry or microwave plasma atomic emission spectrometry.

The width of the nanowires. No relationship is found between the composition of the nanoparticle and the width of the corresponding nanoparticle. In general, the width of SiNWs is a function of the nanoparticle size, as shown in earlier works [3]. Since only the size of CIS and Au nanoparticles were measured, no conclusions can be drawn. However, there is a clear correlation between the mass density of nanoparticles on the carbon substrate and the width of the SiNWs. SEM images confirm that the nanoparticles merge upon heating, creating bigger

liquid metal droplets, which result in wider nanowires. This may be due to Ostwald ripening [4,52]. Small liquid metal droplets evaporate and condensate on the larger droplets.

For further analysis, the sizes of the nanoparticles should be measured using high resolution transmission electron microscopy or X-ray diffraction methods to draw relationships between the seed size and the width of the SiNWs.

Photocurrents. All the carbon substrate samples covered with SiNWs generated photocurrent. However, the repeatability of the results was poor which is probably due to inconsistency of the amount of SiNWs grown in series of the same conditions. The photocathode synthesised using CIS nanoparticles did not surpass the photocurrent of the photocathode synthesised using Au nanoparticles for the samples both with and without catalyst. Although the nanoparticle seeds are different, the shape of the nanowires is the same. The difference probably originates from the smaller size of CIS nanoparticles compared to Au nanoparticles which results in narrower nanowires grown from CIS nanoparticles. Since it is shown that wider nanowires absorb longer wavelengths and a broader part of the solar spectrum [3,53], wider nanowires produce more photocurrent. For comparison, synthesis of CIS seeds should be modified to obtain larger seeds.

Catalyst electrodeposition method was significantly more effective in increasing photocurrent that spray-coating and drop-casting methods which both caused the formation of large catalyst agglomerates on the surface. To avoid this, ink could be ball-milled or treated in sone other way to reduce particle size of the suspension before use. However, the photocurrent obtained with catalyst coating is inferior to an analogous photocathode in literature [3] which might be due to poor SiNW growth or non-optimal catalyst coating. In addition, the maximum photocurrent 16 μA cm^{-2} achieved at −0.15 V vs SHE with a photocathode based on alternative growth seeds is far inferior to best results reported in literature such as 30 or 37 mA cm^{-2} at 0 V vs RHE [27,33].

Finally, the continuous linear sweep voltammetry cycling increased photocurrent significantly. However, the mechanism of this increase is unknown and should be studied further by x-ray photoelectron spectroscopy of the samples to establish the structural changes in the catalyst layer.

The possible error points and the factors affecting the repeatability and consistency of the batches and the results. The main problem affecting the repeatability of the results is the inconsistency of SiNW synthesis across synthesis batches – carbon substrate samples with the same type and amount of nanoparticles grow different amount of SiNWs. This is in conflict with earlier results with Au and SnS nanoparticles, where the process was well

reproducible [2,3]. However, in this work no two synthesis batches of samples were identical. Therefore, the amount of SiNWs grown on a specific sample probably depends also on the concentration and type of seeds on other samples in the same batch. This was specifically noticeable in a batch of 16 Au-based samples and 8 CIS-based samples where CIS-based samples had significantly lower SiNW density than syntheses where the batch consisted of only CIS-based samples. Silane decomposition and solubilisation mechanism probably has preference for certain seeds over others. Some batches included up to 7 different types of seeds at varying concentrations which probably resulted in different amount of SiNWs grown than if every type of seeds were to be used in a separate synthesis batch. Therefore, at this stage of research, the silicon nanowire growth is rather qualitative than quantitative. However, there is no evidence that the morphology of the SiNWs grown from certain seeds is influenced by the different types of seeds in the reactor.

The time between the synthesis and photocurrent measurements may affect photocurrent results. Silicon nanowires have been recorded to oxide in air environment [3]. Although the samples remained in argon glove box whenever possible, the time samples were exposed to air before photocurrent measurements varied for samples from hours up to a few days. To counter this, a passivation layer could be deposited after SiNW synthesis [26,27,32,34].

Summary

A photocathode based on SiNWs was created for water-splitting and coated with amorphous MoS_x catalyst. Metal sulphide quantum dots were employed as novel seeds alternative to conventional metal nanoparticles for the synthesis of SiNWs on porous carbon substrate by chemical vapour deposition method. The investigated nanoparticles were $CuInS_2$, CuInZnS, ZnS, CuS, InS, AgS, CuZns, AgSnS, AgSnZnS, CuSnS, SnInS, and AgInS:Cu. Each constituent metal of the alternative growth seeds contributed different characteristics to grown SiNWs. Cu produced straight, wide and rigid nanowires; In produced twisted and wide nanowires; Sn produced long and wide nanowires, the use of Ag generated bush-like deformities; and Zn was found to have no effect on the morphology of the nanowires nor their photoelectrochemical behaviour. The width of the nanowires was confirmed to have a positive correlation with the concentration of nanoparticles used for synthesis, which occurs due to nanoparticles merging during heating in the synthesis reactor.

Photocathodes with $CuInS_2$-based nanowires were selected for further photoelectrochemical assessment due to their shape's close resemblance to Au-grown nanowires and their favourable silicon to nanoparticle weight ratio. However, the photocathodes with SiNWs synthesised from these novel alternative seeds did not surpass the photocurrent achieved with a photocathode with SiNWs synthesised from Au nanoparticles either with or without a MoS_x catalyst coating. The highest photocurrent obtained with $CuInS_2$ was 16 µA cm^{-2} at −0.15 V vs SHE while the Au counterpart reached 34 µA cm^{-2}, with catalyst coating employed. Both results are below what is reported in the literature. Catalyst drop-casting and spray-coating methods were inefficient at increasing photocurrent compared to electrodeposition method, due to formation of catalyst agglomerates. Photocurrents of InS and CuS-based SiNW photocathodes were inferior to $CuInS_2$-based SiNW photocathode.

Different synthesis batches exhibited deviations in photocurrent results due to the variability in SiNWs synthesis. The growth of SiNWs from one seed is influenced by the presence of other types of seeds in the reactor. Silane decomposition shows a preference for some seeds over others, due to different reaction kinetics and seeds characteristics.

Further studies should include the exact elemental analysis of quantum dots for a complete assessment of the dependence of morphology and size on the seed, the use of passivation layer on the SiNWs, the separation of synthesis batches for each type of alternative seeds for quantitative analysis of SiNWs growth, composition analysis of samples after long-term photocurrent generation, and the treatment of ink for spray-coating and drop-casting methods.

References

[1] A. Fujishima, K. Honda, Electrochemical Photolysis of Water at a Semiconductor Electrode, Nature 238 (1972) 37–38. https://doi.org/10.1038/238037a0.

[2] C. Keller, S. Karuppiah, M. Raaen, J. Wang, P. Perrenot, D. Aldakov, P. Reiss, C. Haon, P. Chenevier, Low-Cost Tin Compounds as Seeds for the Growth of Silicon Nanowire–Graphite Composites Used in High-Performance Lithium-Ion Battery Anodes, ACS Appl. Energy Mater. 6 (2023) 5249–5258. https://doi.org/10.1021/acsaem.3c00178.

[3] J. Wang, C. Keller, M. Dietrich, P.E. Olli, P. Gentile, S. Pouget, H. Okuno, M. Boutghatin, Y. Pennec, V. Reita, D.N. Nguyen, H. Johnson, A. Morozan, V. Artero, P. Chenevier, Porous silicon-nanowire-based electrode for the photoelectrocatalytic production of hydrogen, Sustainable Energy Fuels 7 (2023) 4864–4876. https://doi.org/10.1039/D3SE00408B.

[4] V. Schmidt, J.V. Wittemann, S. Senz, U. Gösele, Silicon Nanowires: A Review on Aspects of their Growth and their Electrical Properties, Adv. Mater. 21 (2009) 2681–2702. https://doi.org/10.1002/adma.200803754.

[5] C.G. Morales-Guio, X. Hu, Amorphous Molybdenum Sulfides as Hydrogen Evolution Catalysts, Acc. Chem. Res. 47 (2014) 2671–2681. https://doi.org/10.1021/ar5002022.

[6] M.G. Walter, E.L. Warren, J.R. McKone, S.W. Boettcher, Q. Mi, E.A. Santori, N.S. Lewis, Solar Water Splitting Cells, Chem. Rev. 110 (2010) 6446–6473. https://doi.org/10.1021/cr1002326.

[7] T.R. Anderson, E. Hawkins, P.D. Jones, CO2, the greenhouse effect and global warming: from the pioneering work of Arrhenius and Callendar to today's Earth System Models, Endeavour 40 (2016) 178–187. https://doi.org/10.1016/j.endeavour.2016.07.002.

[8] A. Dosio, L. Mentaschi, E.M. Fischer, K. Wyser, Extreme heat waves under 1.5 °C and 2 °C global warming, Environ. Res. Lett. 13 (2018) 054006. https://doi.org/10.1088/1748-9326/aab827.

[9] J.W. Erisman, M.A. Sutton, J. Galloway, Z. Klimont, W. Winiwarter, How a century of ammonia synthesis changed the world, Nature Geosci 1 (2008) 636–639. https://doi.org/10.1038/ngeo325.

[10] C. Cunanan, M.-K. Tran, Y. Lee, S. Kwok, V. Leung, M. Fowler, A Review of Heavy-Duty Vehicle Powertrain Technologies: Diesel Engine Vehicles, Battery Electric Vehicles, and Hydrogen Fuel Cell Electric Vehicles, Clean Technologies 3 (2021) 474–489. https://doi.org/10.3390/cleantechnol3020028.

[11] N. Gray, S. McDonagh, R. O'Shea, B. Smyth, J.D. Murphy, Decarbonising ships, planes and trucks: An analysis of suitable low-carbon fuels for the maritime, aviation and haulage sectors, Adv. Appl. Energy 1 (2021) 100008. https://doi.org/10.1016/j.adapen.2021.100008.

[12] International Energy Agency, Energy Technology Perspectives 2017, Paris, 2017. https://www.iea.org/reports/energy-technology-perspectives-2017.

[13] A.J. Pimm, T.T. Cockerill, W.F. Gale, Energy system requirements of fossil-free steelmaking using hydrogen direct reduction, J. Clean. Prod. 312 (2021) 127665. https://doi.org/10.1016/j.jclepro.2021.127665.

[14] F. Williams, A. Yang, D.R. Nhuchhen, Decarbonisation pathways of the cement production process via hydrogen and oxy-combustion, Energy Convers. Manag. 300 (2024) 117931. https://doi.org/10.1016/j.enconman.2023.117931.

[15] A. Nemmour, A. Inayat, I. Janajreh, C. Ghenai, Green hydrogen-based E-fuels (E-methane, E-methanol, E-ammonia) to support clean energy transition: A literature review, Int. J. Hydrog. Energy 48 (2023) 29011–29033. https://doi.org/10.1016/j.ijhydene.2023.03.240.

[16] J. Wakefield, M. Kassem, Improving Site Access Verification and Operator Safety in Smart and Sustainable Cities: A Pilot Study in A UK Decarbonisation Project., in: 2020: pp. 374–384. https://doi.org/10.46421/2706-6568.37.2020.paper027.

[17] P. p Edwards, V. l Kuznetsov, W. i. f David, Hydrogen energy, Phil. Trans. R. Soc. A 365 (2007) 1043–1056. https://doi.org/10.1098/rsta.2006.1965.

[18] R. Palm, H. Kurig, J. Aruväli, E. Lust, NaAlH4/microporous carbon composite materials for reversible hydrogen storage, Microporous Mesoporous Mater. 264 (2018) 8–12. https://doi.org/10.1016/j.micromeso.2017.12.027.

[19] R. Van De Krol, M. Grätzel, Introduction, in: R. Van De Krol, M. Grätzel (Eds.), Photoelectrochemical Hydrogen Production, Springer US, Boston, MA, 2012: pp. 3–11. https://doi.org/10.1007/978-1-4614-1380-6_1.

[20] H. Wu, Hui Ling Tan, C.Y. Toe, J. Scott, L. Wang, R. Amal, Y.H. Ng, Photocatalytic and Photoelectrochemical Systems: Similarities and Differences, Adv. Mater. 32 (2020) 1904717. https://doi.org/10.1002/adma.201904717.

[21] R. Van De Krol, M. Grätzel, eds., Photoelectrochemical Hydrogen Production, Springer US, Boston, MA, 2012. https://doi.org/10.1007/978-1-4614-1380-6.

[22] K. Sun, S. Shen, Y. Liang, P.E. Burrows, S.S. Mao, D. Wang, Enabling silicon for solar-fuel production, Chem Rev 114 (2014) 8662–8719. https://doi.org/10.1021/cr300459q.

[23] M. Grätzel, Photoelectrochemical cells, Nature 414 (2001) 338–344. https://doi.org/10.1038/35104607.

[24] M.S. Wrighton, Photoelectrochemical conversion of optical energy to electricity and fuels, Acc. Chem. Res. 12 (1979) 303–310. https://doi.org/10.1021/ar50141a001.

[25] F. E. Osterloh, Inorganic nanostructures for photoelectrochemical and photocatalytic water splitting, Chem. Soc. Rev. 42 (2013) 2294–2320. https://doi.org/10.1039/C2CS35266D.

[26] R. Fan, W. Dong, L. Fang, F. Zheng, X. Su, S. Zou, J. Huang, X. Wang, M. Shen, Stable and efficient multi-crystalline n+p silicon photocathode for H2 production with pyramid-like surface nanostructure and thin Al2O3 protective layer, Appl. Phys. Lett. 106 (2015) 013902. https://doi.org/10.1063/1.4905511.

[27] M.H. Lee, K. Takei, J. Zhang, R. Kapadia, M. Zheng, Y. Chen, J. Nah, T.S. Matthews, Y. Chueh, J.W. Ager, A. Javey, p-Type InP Nanopillar Photocathodes for Efficient Solar-Driven Hydrogen Production, Angew Chem Int Ed 51 (2012) 10760–10764. https://doi.org/10.1002/anie.201203174.

[28] Y. Nakato, T. Ohnishi, H. Tsubomura, Photo-Electrochemical Behaviours of Semiconductor Electrodes Coated With Thin Metal Films, Chem. Lett. 4 (1975) 883–886. https://doi.org/10.1246/cl.1975.883.

[29] Y. Nakato, H. Tsubomura, Silicon photoelectrodes modified with ultrafine metal islands, Electrochim. Acta 37 (1992) 897–907. https://doi.org/10.1016/0013-4686(92)85041-I.

[30] A. Heller, E. Aharon-Shalom, W.A. Bonner, B. Miller, Hydrogen-evolving semiconductor photocathodes: nature of the junction and function of the platinum group metal catalyst, J. Am. Chem. Soc. 104 (1982) 6942–6948. https://doi.org/10.1021/ja00389a010.

[31] J.D. Benck, T.R. Hellstern, J. Kibsgaard, P. Chakthranont, T.F. Jaramillo, Catalyzing the Hydrogen Evolution Reaction (HER) with Molybdenum Sulfide Nanomaterials, ACS Catal. 4 (2014) 3957–3971. https://doi.org/10.1021/cs500923c.

[32] J. Gu, J.A. Aguiar, S. Ferrere, K.X. Steirer, Y. Yan, C. Xiao, J.L. Young, M. Al-Jassim, N.R. Neale, J.A. Turner, A graded catalytic-protective layer for an efficient and stable water-splitting photocathode, Nat. Energy 2 (2017) 16192. https://doi.org/10.1038/nenergy.2016.192.

[33] H. Kumagai, T. Minegishi, N. Sato, T. Yamada, J. Kubota, K. Domen, Efficient solar hydrogen production from neutral electrolytes using surface-modified Cu(In,Ga)Se 2

photocathodes, J. Mater. Chem. A 3 (2015) 8300–8307. https://doi.org/10.1039/C5TA01058F.

[34] R. Van De Krol, Photoelectrochemical Measurements, in: R. Van De Krol, M. Grätzel (Eds.), Photoelectrochemical Hydrogen Production, Springer US, Boston, MA, 2012: pp. 69–117. https://doi.org/10.1007/978-1-4614-1380-6_3.

[35] Y. Cui, C.M. Lieber, Functional Nanoscale Electronic Devices Assembled Using Silicon Nanowire Building Blocks, Science 291 (2001) 851–853. https://doi.org/10.1126/science.291.5505.851.

[36] M.D. Kelzenberg, D.B. Turner-Evans, B.M. Kayes, M.A. Filler, M.C. Putnam, N.S. Lewis, H.A. Atwater, Photovoltaic Measurements in Single-Nanowire Silicon Solar Cells, Nano Lett. 8 (2008) 710–714. https://doi.org/10.1021/nl072622p.

[37] S. Karuppiah, C. Keller, P. Kumar, P.-H. Jouneau, D. Aldakov, J.-B. Ducros, G. Lapertot, P. Chenevier, C. Haon, A Scalable Silicon Nanowires-Grown-On-Graphite Composite for High-Energy Lithium Batteries, ACS Nano 14 (2020) 12006–12015. https://doi.org/10.1021/acsnano.0c05198.

[38] Y. Bencheikh, M. Harnois, R. Jijie, A. Addad, P. Roussel, S. Szunerits, T. Hadjersi, S. El Hak Abaidia, R. Boukherroub, High performance silicon nanowires/ruthenium nanoparticles micro-supercapacitors, Electrochim. Acta 311 (2019) 150–159. https://doi.org/10.1016/j.electacta.2019.04.083.

[39] Z. Gao, A. Agarwal, A.D. Trigg, N. Singh, C. Fang, C.-H. Tung, Y. Fan, K.D. Buddharaju, J. Kong, Silicon Nanowire Arrays for Label-Free Detection of DNA, Anal. Chem. 79 (2007) 3291–3297. https://doi.org/10.1021/ac061808q.

[40] A.A. Leonardi, M.J.L. Faro, A. Irrera, Silicon Nanowires Synthesis by Metal-Assisted Chemical Etching: A Review, Nanomaterials 11 (2021) 383. https://doi.org/10.3390/nano11020383.

[41] R.S. Wagner, W.C. Ellis, Vapor-Liquid-Solid Mechanism of Single Crystal Growth, Appl. Phys. Lett. 4 (1964) 89–90. https://doi.org/10.1063/1.1753975.

[42] V.G. Dubrovskii, N.V. Sibirev, J.C. Harmand, F. Glas, Growth kinetics and crystal structure of semiconductor nanowires, Phys. Rev. B 78 (2008) 235301. https://doi.org/10.1103/PhysRevB.78.235301.

[43] F.P. García de Arquer, D.V. Talapin, V.I. Klimov, Y. Arakawa, M. Bayer, E.H. Sargent, Semiconductor quantum dots: Technological progress and future challenges, Science 373 (2021) eaaz8541. https://doi.org/10.1126/science.aaz8541.

[44] K. Agarwal, H. Rai, S. Mondal, Quantum dots: an overview of synthesis, properties, and applications, Mater. Res. Express 10 (2023) 062001. https://doi.org/10.1088/2053-1591/acda17.

[45] Y. Xu, T. Chen, X. Hu, W. Jiang, L. Wang, W. Jiang, J. Liu, The off-stoichiometry effect on the optical properties of water-soluble copper indium zinc sulfide quantum dots, J. Colloid Interface Sci. 496 (2017) 479–486. https://doi.org/10.1016/j.jcis.2017.02.049.

[46] Y. Chen, S. Li, L. Huang, D. Pan, Green and Facile Synthesis of Water-Soluble Cu–In–S/ZnS Core/Shell Quantum Dots, Inorg. Chem. 52 (2013) 7819–7821. https://doi.org/10.1021/ic400083w.

[47] Y. Wang, L. Liu, Q. Wang, S. Hu, P. Zou, J. Shi, X. Zhang, Optimization of the aqueous synthesis of Cu2S quantum dots with different surface ligands, Nanotechnology 27 (2015) 015705. https://doi.org/10.1088/0957-4484/27/1/015705.

[48] H. Do Thi, L. Nghien Thi Ha, H. Chu Viet, Seeded Growth Synthesis of Uniform Gold Nanoparticles with Controlled Diameters up to 220 nm, J. Electron. Mater. 50 (2021) 5514–5521. https://doi.org/10.1007/s11664-021-09081-6.

[49] J. Turkevich, P.C. Stevenson, J. Hillier, A study of the nucleation and growth processes in the synthesis of colloidal gold, Discuss. Faraday Soc. 11 (1951) 55–75. https://doi.org/10.1039/DF9511100055.

[50] A. Tabrizi, F. Ayhan, H. Ayhan, Gold Nanoparticle Synthesis and Characterisation, HJBC 37 (2009) 217–226.

[51] J.E. O'Reilly, Oxidation-reduction potential of the ferro-ferricyanide system in buffer solutions, Biochimica et Biophysica Acta (BBA) - Bioenergetics 292 (1973) 509–515. https://doi.org/10.1016/0005-2728(73)90001-7.

[52] W. Ostwald, Lehrbuch der allgemeinen chemie, Leipzig, W. Engelmann, 1885. http://archive.org/details/lehrbuchderallg04ostwgoog (accessed May 27, 2024).

[53] T. Xu, Y. Lambert, C. Krzeminski, B. Grandidier, D. Stiévenard, G. Lévêque, A. Akjouj, Y. Pennec, B. Djafari-Rouhani, Optical absorption of silicon nanowires, J. Appl. Phys. 112 (2012) 033506. https://doi.org/10.1063/1.4739708.

Acknowledgements

First and foremost, the author wishes to thank his supervisors Pascale Chenevier and Jaak Nerut. Many thanks to Djamilla Chou for helping with the synthesis of quantum dots and to Omar El-Dahshan for providing AgS quantum dots. In addition, deep gratitude goes towards for Adina Morozan, Peter Reiss and Celine Rivaux for the support while conducting the experiments. Warm greetings to all the people at the STEP laboratory. Special thanks go to Annabel Olgo and Ove Korjus for the emotional support.

This work was financially supported by European Horizon 2020's Project Sun-to-X under agreement no. 883264, University of Tartu (Experimental Development Grant Novel Catalysts for Alkaline Electrolyser Electrodes Based on Nickel Foam), the project ”Increasing the knowledge intensity of Ida-Viru entrepreneurship” co-funded by the European Union (ÕÜF1) and the Estonian Ministry of Education and Research (Center of Excellence TK210).

Supplementary

Supplementary 1. Summary in Estonian

KOKKUVÕTE

Alternatiivsetest kristallatsioonitsentritest kasvatatud räni-nanotraatidel põhinev fotokatood vesiniku fotoelektrokatalüüsiks

Fossiilsete energiaallikate kasutamine põhjustab kliima soojenemist ning ekstreemsete ilmastikuolude intensiivistumist, mis on sundinud riike ümber korraldama oma energiamajandust ning leidma uusi alternatiivseid energiaallikaid.

Vesinik on tugev kandidaat uue aja energiamajanduse tsentraalseks energiakandjaks. Esiteks on vesinikul eriti suur energiatihedus (33,3 kWh kg^{-1}) võrreldes fossiilsete energiakandjatega, näiteks bensiiniga (12,8 kWh kg^{-1}). Teiseks on võimalik vesinikuga asendada fossiilsed energiaallikad rakendustes, kus rohelist elektrienergiat otse kasutada ei saaks, nagu rasketransport või tsemendi- ja terasetööstus, mis kahe peale kokku tekitavad praegu 14% maailma süsihappegaasi heidetest. Kolmandaks on vesinik mitmeotstarbeline energiakandja, mida saab kütuselementidega muuta elektriks või sünteesida koos õhu süsihappegaasiga traditsiooniliste fossiilsete energiakandjatega keemiliselt identseid e-kütuseid, mida on lihtne kasutada juba olemasolevas infrastruktuuris.

Rohelist vesinikku, mis ei pärine fossiilsetest allikatest, toodetakse vee elektrolüüsi teel elektrolüüserites, kasutades rohelist elektrit. Kui rohelist elektrist saadakse näiteks päikeseenergiast päikesepaneele kasutades, siis on võimalik muundada päikeseenergia vesinikuenergiaks umbes 15% efektiivsusega. Samas võiks teoreetiliselt muutuda protsess efektiivsemaks kui toota vesinikku vahetult päikeseenergiast, kasutades fotoelektrokatalüütilist vee lõhustamist.

Fotoelektrokatalüütiliseks vee lõhustamiseks kasutatakse pooljuhte, nagu räni või indium, mis neelavad footoneid. Footoni neelamisel ergastub pooljuhis elektron valentstsoonist juhtivustsooni ning ergastunud footoni energiat saab kasutada, et läbi viia elektrokeemilisi reaktsioone, nagu vee lagunemine. Et vähendada vee lagunemise reaktsiooniks vajalikku energiat, saab reaktsiooni läbi viia kahel eraldi fotoelektroodil: vesiniku redutseerimine fotokatoodil ja vee oksüdeerimine fotoanoodil.

Nanostruktureeritud fotoelektroodil on mitmeid eeliseid tasapinnaliste fotoelektroodi ees – näiteks suurem valguse hajumine fotoelektroodi sees, mis vähendab valguse peegeldumist ja suurendab valguse neeldumist. Teiseks on elektroodil suurem pindala, mis suurendab võimalike

reaktsioonitsentride arvu. Lisaks saab tänu kvantefektidele muuta nanostruktuuriga pooljuhtide ergastusenergiat, modifitseerides nano-osakese suurust.

Räni-nanotraadid on nanostruktuurid, mille levinuim sünteesimeetod on keemiline aurufaasi sadestamine. Nano-osakestest kristallatsioonitsentreid, näiteks kulla nano-osakesi, kuumutatakse reaktoris koos gaasilise räni prekursoriga, näiteks $SiCl_4$ või SiH_4, mis laguneb ning räni lahustub nanoosakese sisse, moodustades sulami. Räni küllastumisel nano-osakeses hakkab räni nanoosakesest välja kristalliseeruma, moodustades räni-nanotraadid.

Kulla ja teiste metallide nano-osakestega on keeruline saavutada homogeense suurusega nanotraate. Lisaks on kuld kallis. Alternatiivina on uuritud sulfiidsete kvanttäppide kasutamist kristallatsioonitsentritena. Kvanttäpid on kvantomadustega pooljuhtide väikeste mõõtmetega (kuni 20 nm) nano-osakesed, mis on ümbritsetud orgaaniliste liganditega, mis aitavad vältida kvant-täppide aglomeerumist. Sulfiidsed kvanttäpid lagunevad kuumutamisel ning alles jääb vaid vedel sulam. Varem on räni-nanotraatide sünteesiks edukalt kasutatud tinasulfiidi nano-osakesi räni-nanotraatide sünteesiks.

Käeolevas uurimustöös sünteesiti räni-nanotraate, kasutades kristallatsioonitsentritena uudseid kvanttäppe, et leida alternatiiv laialdaselt kasutatavatele kulla nano-osakestele. Poorsele süsinikkandjale sünteesitud räni-nanotraatide komposiitmaterjali kasutati vesiniku fotoelektrokatalüüsi fotokatoodina.

Uurimistöö eesmärgid olid:

1) Sünteesida ja uurida uudseid kirstallatsioonitsentreid, mis asendaksid kulla nano-osakesi räni nanotraatide sünteesis keemilise auru faasi sadestusmeetodil, kasutades prekursorina difenüülsilaani
2) Karakteriseerida räni nanotraate, mis on kasvatatud alternatiivsetest kristallatsioonitsentritest
3) Hinnata räni nanotraatidel põhinevat ning molübdeensulfiidi katalüsaatoriga kaetud fotokatoodi fotoelektrokeemilist võimekust

Räni-nanotraaatide sünteesiks kasutatud kvanttäpid olid nano-mõõtmetes (kuni 20 nm) mono-, bi- ja trisulfiidid, mille metalliliseks koostisosaks olid Cu, In, Zn, Ag ja Sn kombinatsioonid ($CuInS_2$, CuInZnS, ZnS, CuS, In_2S_3, AgS, CuZn, AgSnS, AgSnZnS, CuSnS, SnInS, ja AgInS:Cu). Räni-nanotraate kasvatati argooniga täidetud reaktoris 430 °C ja 16 baari juures 3-4 tundi ning lähteainetena kasutati difenüülsilaani. Elektronmikroskoobi piltidelt selgus, et räni-nanotraatide kuju ja diameeter sõltub kasutatud kvanttäppide keemilisest koostisest ning kogusest. Iga metall mõjutab traatide kuju erinevalt ning elementide kombineerimine võimaldab räni-nanotraatid omadusi varieerida vastavalt soovile. Vase

sisaldus kvanttäpis andis nanotraatidele sirge kuju, kuid puhtad CuS osakesed degradeerusid kiiresti ning olid seega kasutamiseks ebapraktilised. Indiumi sisaldus kvanttäpis muutis nanotraadid sakiliseks ning jämedaks. Tsink ei avaldanud mõju nanotraatide morfoloogiale ning ZnS osakesed olid liiga stabiilsed räni-nanotraatide sünteesi jaoks. Tina sisaldus tekitas pikad ja selgelt eristuvad nanotraadid ning hõbeda sisaldus kvanttäppides põhjustas selgete traatide asemel svamjate kogumite moodustumist. AgS osakestega ei õnnestunud räni-nanotraate sünteesida.

Nanotraatide diameeter korrelleerub nano-osakeste tihedusega, mis tuleneb nano-osakeste kokkusulamisest kõrgel temperatuuril sünteesireaktoris. Lisaks kujule ja suurusele varieerus nanotraatide ja nano-osakeste massisuhe. Kvanttäpid nagu In_2S_3 ja AgSnS olid kasutamiseks sobimatud, sest soovitud koguse räni-nanotraatide sünteesi jaoks kulus liiga suur kogus kvanttäppe.

Vee lõhustamise fotoelektrokeemilise fotokatoodi jaoks valiti välja $CuInS_2$ kvant-täppidega sünteesitud nanotraadid, sest need sarnanesid kujult kulla nano-osakestest sünteesitud nanotraatidega (sirged, homogeensed, ämblikuvõrku meenutavate mikrostruktuuridega) ning nanotraatide ja nano-osakeste suhe oli uuritud kvant-täppide seas kõrgeim. Kuigi mitmed sünteesitud nanotraadid ei ole kuju tõttu fotoelektrokatalüüsi jaoks sobilikud, võivad need sobida kasutamiseks teistes rakendustes, näiteks liitiumioonakudes.

Fotokatoodi loomiseks sünteesiti nanotraadid süsinikkandjale. Selleks kasutati vesiniku kütuselementides kasutatavat poorset ja kõrge elektrijuhtivusega Freudenbergi gaasidiffusioonikihti. Fotokatoodile sadestati kolmel eri meetodil MoS_x katalüsaatorit, et kiirendada vesiniku eraldumise reaktsiooni. MoS_x suspensiooni elektroodile kandmine tilgutusmeetodil ja pihustusmeetodil andis elektrosadestusmeetodiga võrreldes väikese katalüütilise efekti. Selle põhjuseks on fotokatoodi pinnale tekkinud suured katalüsaatori aglomeraadid, mille eripind on väike võrreldes soovitud väikeste osakestega. Seega peaks suspensiooni enne kasutamist töötlema näiteks kuulveskis. Katalüsaatori elektrosadestamine pingel 0,1 V vs SHE (standardne vesinikelektrood) ja laengutihedusel 6.0 mC cm^{-2} suurendas fotovoolu märgatavalt. Ilma katalüsaatorita oli fotovool 0.86 µA cm^{-2}. Tilgutusmeetodiga ning pihustusmeetodiga saavutati vastavalt 4.2 ja 3.6 µA cm^{-2}, kuid elektrosadestamisega 15 µA cm^{-2}. Alternatiivsete nano-osakeste korral ei suudetud ületada kulla nano-osakestel kasvatatud nanotraatide fotokatoodi fotovoolu. Katalüsaatoriga küündis kulla nano-osakestel põhineva fotokatoodi fotovool väärtuseni 34 µA cm^{-2}. Nõrgem tulemus võib olla tingitud kahest asjaolust. Esiteks kasvatasid kulla nano-osakesed suurema koguse nanotraate, sest kuld on efektiivsem kristallatsioonitsenter kui kvanttäpid. Teiseks olid sünteesitud $CuInS_2$ kvanttäpid

17 nm surused, kuid kasutatud kulla nano-osakeste läbimõõt oli 55 nm. Kvanttäppide väikeste mõõtmete tõttu on ka kasvanud nanotraadid väiksema diameetriga. Seetõttu on saadav fotovool väiksem, sest suurema diameetriga nanotraadid neelavad suurema osa päikesevalguse spektrist. Edasises uurimistöös peaks uurima kullaga sarnaselt kvant-täppide suuremaks kasvatamise võimalusi.

Probleemiks kujunes räni-nanotraatide seeriate korratavus. Samade kvanttäppidega ja samadel kvanttäppide kogusega sünteesitud räni-nanotorudega fotokatoodid andsid erinevaid fotovoolu tulemusi. See tulenes sellest, et räni-nanotraatide kasvu hulk ühel proovil sõltus ka teistest sünteesireaktoris olevatest proovidest. Kui reaktoris oli kahte eri tüüpi nano-osakesi, siis vähem aktiivsetel nano-osakestel kasvas väiksem mass nanotraate kui oleks kasvanud siis, kui reaktoris oleks olnud vaid vähem aktiivsed nano-osakesed. Sellest tulenevalt on võimalik luua kasutatud kristallatsioonitsentrite hierarhia selle alusel, millisel kristallatsioonitsentril räni lähteaine kõige kiiremini laguneb. Hierarhia tipus on kulla nanoosakesed ja $CuInS_2$ kvanttäpid ning hierarhia viimasel astmel In_2S_3 kvanttäpid.

Täideti edukalt kõik töö eesmärgid. Uuriti alternatiivseid kristallatsioonitsentreid ning selgitati välja nende sobivus räni nanotraatide sünteesiks. Karakteriseeriti alternatiivsetest kristallatsioonitsentritest kasvatatud räni nanotraate. Hinnati kasvatatud räni nanotraatidel põhineva ning molübdeensulfiid-katalüsaatoriga kaetud fotokatoodi fotoelektrokeemilist võimekust.

Supplementary 2. Used reagents

Table S2. The reagents used to synthesise nanoparticles and silicon nanowires.

Chemical Name	Chemical Formula	Provider	Purity
Sodium sulfide nonahydrate	$Na_2S \times 9\ H_2O$	Acros organics	98+%
Sodium hydroxide	NaOH	Sigma Aldrich	1.0 N solution
L-Glutathione	$C_{10}H_{17}N_3O_6S$	Sigma Aldrich	≥ 98%
Thioglycolic acid	$C_2H_4O2_S$	Sigma Aldrich	≥ 99%
Indium (III) Chloride	$InCl_3$	Sigma Aldrich	99.999%
Copper (II) chloride hydrate	$CuCl_2 \times H_2O$	Thermofischer	99.999%
Zinc (II) acetate hydrate	$Zn(CH_3COO)_2 \times H_2O$	Alfa Aesar	> 97%
Water	H_2O	MilliQ	Conductivity 18.2 MΩ cm-1 at 25 °C
Silver nitrate	$AgNO_3$	Thermofisher	> 99.9%
Copper (II) nitrate trihydrate	$Cu(NO_3)_2 \times 3H_2O$	Acros organics	99%
Copper (I) bromide	CuBr	Sigma Aldrich	≥ 98.0%
Isopropanol	$(CH_3)_2CHOH$	Carlo Erba	99.9%
Absolute ethanol	C_2H_5OH	Carlo Erba	≥ 99.9%
Thiourea	$SC(NH_2)_2$	Alfa Aesar	> 99%
Ammonium hydroxide	NH_4OH	Carlo Erba	28%
Nitric acid	HNO_3	Carlo Erba	65.0±1.0%
Citric acid	$C_6H_8O_7$	Sigma Aldrich	99%
Gold (III) chloride hydrate	$HAuCl_4 \times x\ H_2O$	Sigma Aldrich	-
Sodium citrate tribasic dihydrate	$Na_3C_6H_5O_7 \times 2\ H_2O$	Sigma Aldrich	≥ 99.0%
Ascorbic acid	$C_6H_8O_6$	Sigma Aldrich	Reagent grade
Hydrochloric acid	HCl	Acros Organics	37% (36 – 38%)
Diphenylsilane	$C_{12}H_{12}Si$	Chemicalpoint	Purity unknown
Acetonitrile	C_2H_3N	Fisher chemicals	99.998%
Acetone	C_3H_6O	Carlo Erba	99.8%
Dichloromethane	CH_2Cl_2	Carlo Erba	99.9%
Propan-2-ol	C3H8O	Carlo Erba	≥ 99.9%
Nanoparticles	-	Synthesized by the author and co-workers	-

Supplementary 3. Scanning electron microscopy images of nanoparticles

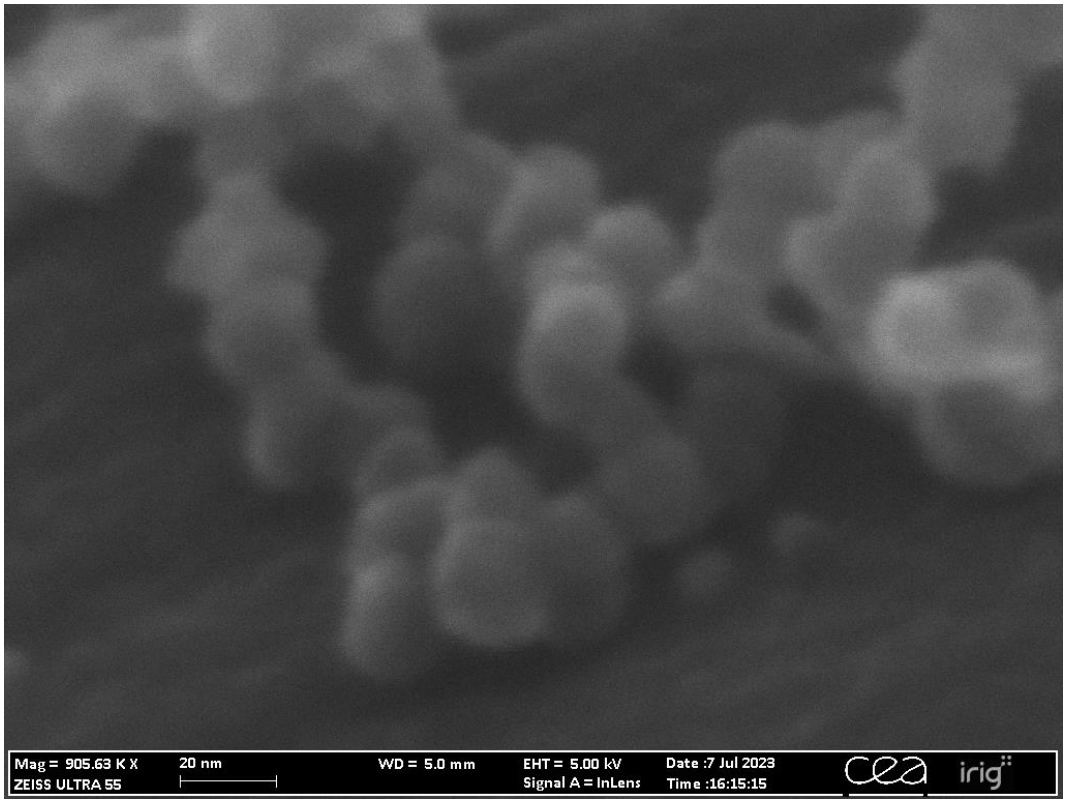

Figure S3.1 CIS nanoparticles deposited on carbon fibres. SEM images confirmed the size to be 18 (±5) nm.

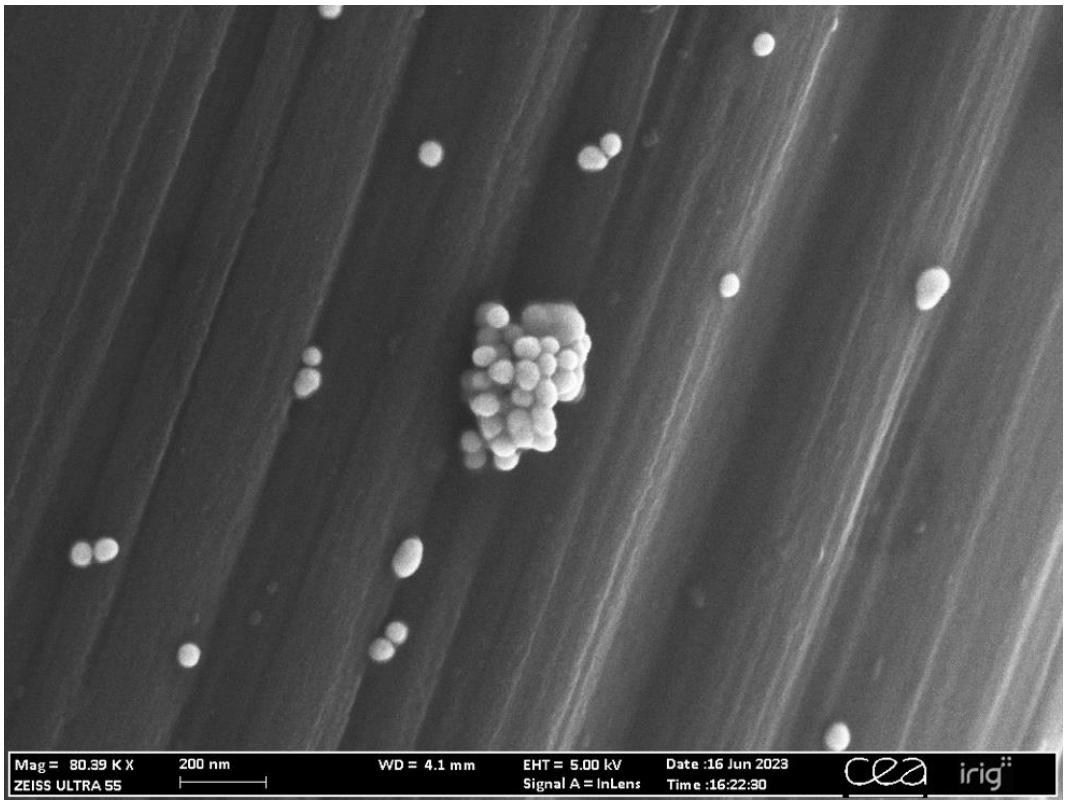

Figure S3.2. 80-nm sized Au nanoparticles deposited on carbon gas diffusion layer after synthesis. SEM images confirmed the actual size of the nanoparticles to be 55 (±8) nm.

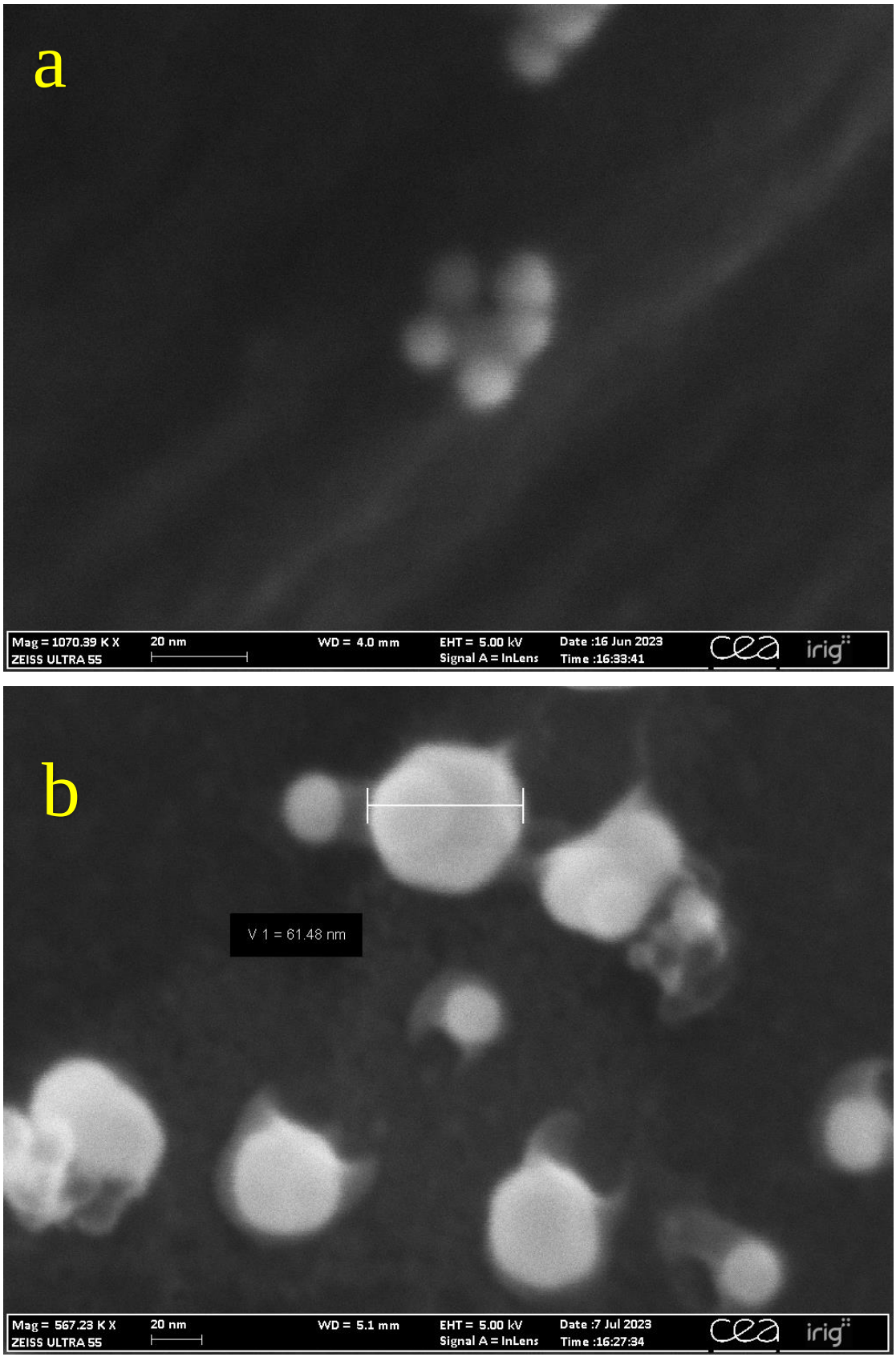

Figure S3.3. 12-nm sized Au nanoparticles deposited on carbon gas diffusion layer before heating (a) and after being exposed to 430 °C for 4 hours. Scanning electron microscopy images confirmed the size of the nanoparticles after heating to be 39 (±20) nm.

Supplementary 4. Specification of synthesis batches

Table S4.1. Specification of samples in synthesis batches 5-6. Each batch consisted of 20-24 carbon gas diffusion layer samples, each measuring 2.54 × 0.635 cm. The nanoparticles were deposited onto the gas diffusion layer samples at loadings specified in the table. The samples were then enclosed in the synthesis reactor. Inside the reactor, elevated temperatures and pressure initiated silicon nanowire growth in the presence of diphenylsilane.

Batch number	Batch 1	Batch 2	Batch 3	Batch 4	Batch 5	Batch 6
Nano-particle	CIS (6 loadings)	CIS (10 loadings)	CIS (20 loadings)	Au (16 loadings)	Ag_2S (5 loadings)	In_2S_3 (6 loadings)
Nano-particle loadings (µg cm^{-2})	12 25 37 50 62 74	37 37 43 43 50 50 56 56 62 62	25 56 43 56 43 56 50 62 50 62 56 74 56 74 56 87 56 87 56 105	25 87 25 87 50 99 50 99 62 120 62 120 74 150 74 150	25 43 56 68 87	310 620 930 1200 1600 1900
Nano-particle	CIZS (8 loadings)	CIZS (10 loadings)		CIS (8 loadings)	Cu_2S (5 loadings)	Cu_2S (3 loadings)
Nano-particle loadings (µg cm^{-2})	12 25 4 37 6 50 12 62	31 43 31 50 37 50 37 56 43 56		25 87 50 99 62 124 74 149	25 43 56 68 87	62 190 310
Nano-particle	ZnS (3 loadings)	ZnS (1 loading)			In_2S_3 (5 loadings)	AgSnZnS (3 loadings)
Nano-particle loadings (µg cm^{-2})	62 190 250	270			25 43 56 68 1600	62 190 560
Nano-particle	CIS spray-coat (4 loadings)				CuZnS (5 loadings)	CuSnS (3 loadings)
Nano-particle loadings (µg cm^{-2})					25 43 56 68 87	62 190 560
Nano-particle						SnInS (3 loadings)
Nano-particle loadings (µg cm^{-2})						62 190 560
Nano-particle						AgSnS (3 loadings)
Nano-particle loadings (µg cm^{-2})						62 190 500
Nano-particle						AgInS:Cu (3 loadings)
Nano-particle loadings (µg cm^{-2})						62 190 560

Supplementary 5. Photocurrent calculation

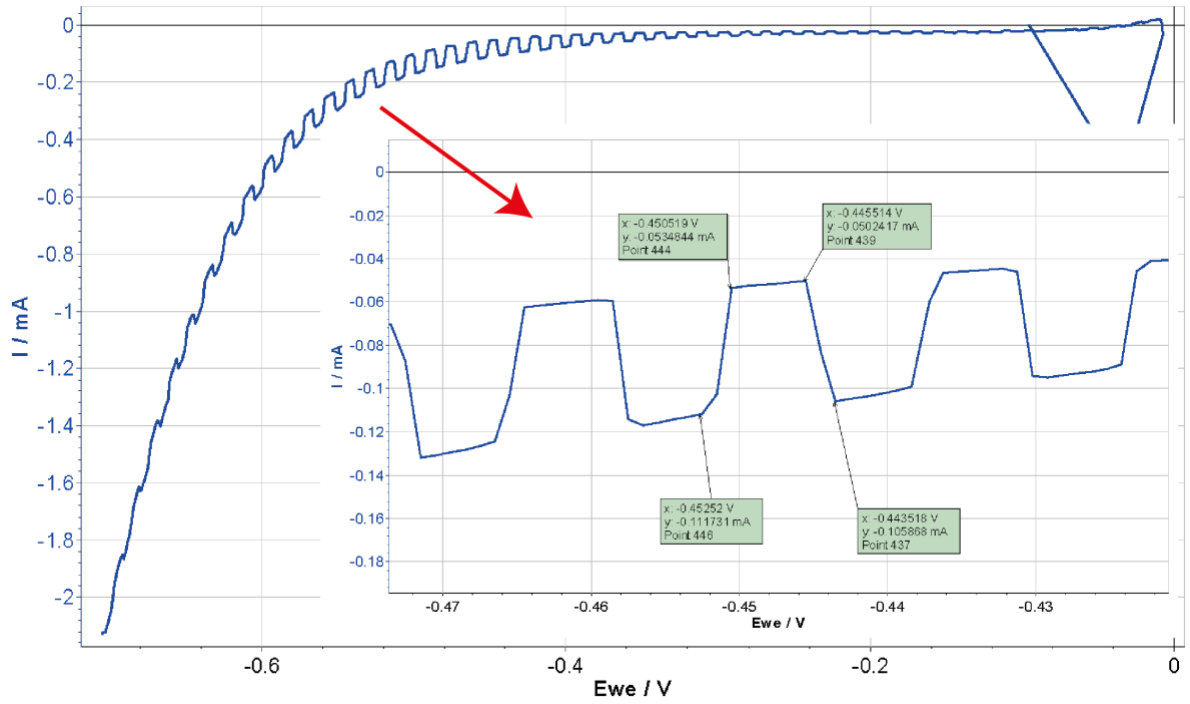

Figure S5.1 Photocurrent calculation method. Photoelectric current was measured from the fluctuating light graph as the average of current differences of two closest light to dark and dark to light transitions closest to the desired potential. The low cathodic current of the spikes, meaning the highs of the spikes, is during dark conditions and high cathodic current, meaning the lows of the spikes, during light conditions. Averaging two differences is necessary to cancel out the general trend of current increase as potential increases. In this example, the photocurrent is 0.5×(0.111+0.106-0.0535-0.0502)=0.0567 mA. Knowing the area of the electrode, current density of the photocathode can be calculated.

Supplementary 6. Scanning electron microscopy images of silicon nanowires

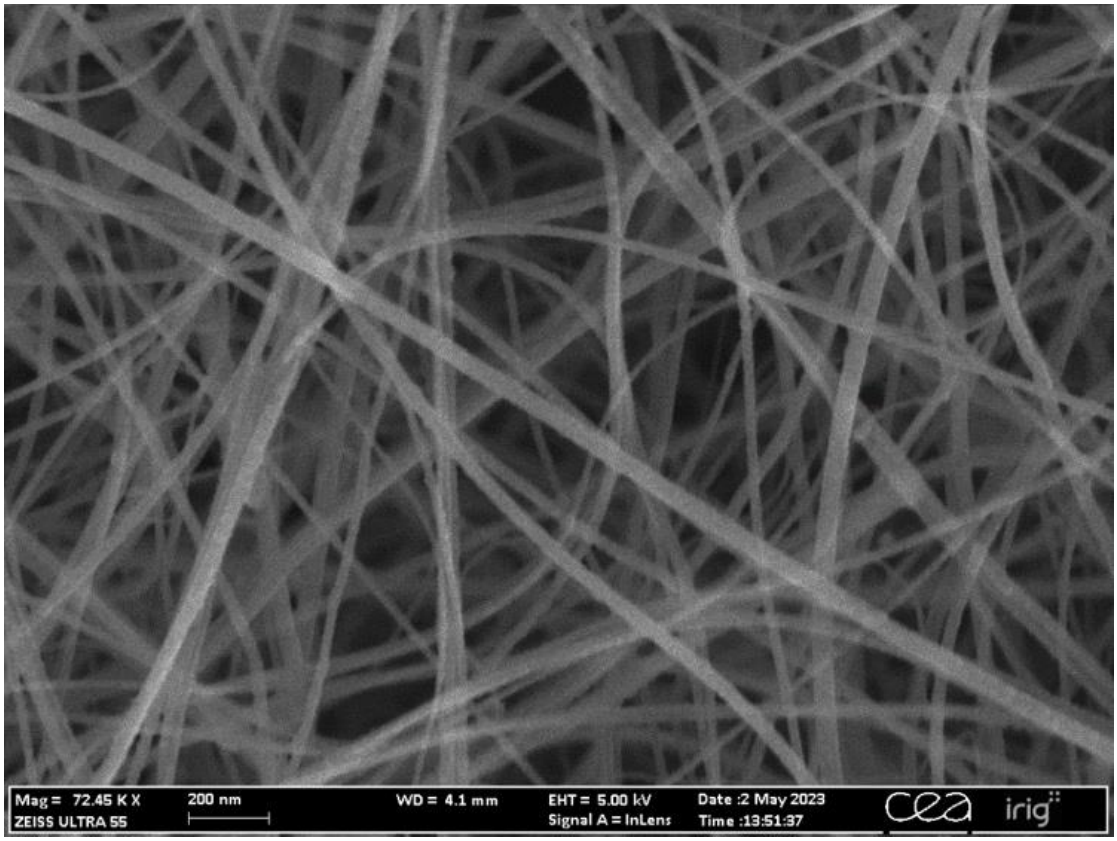

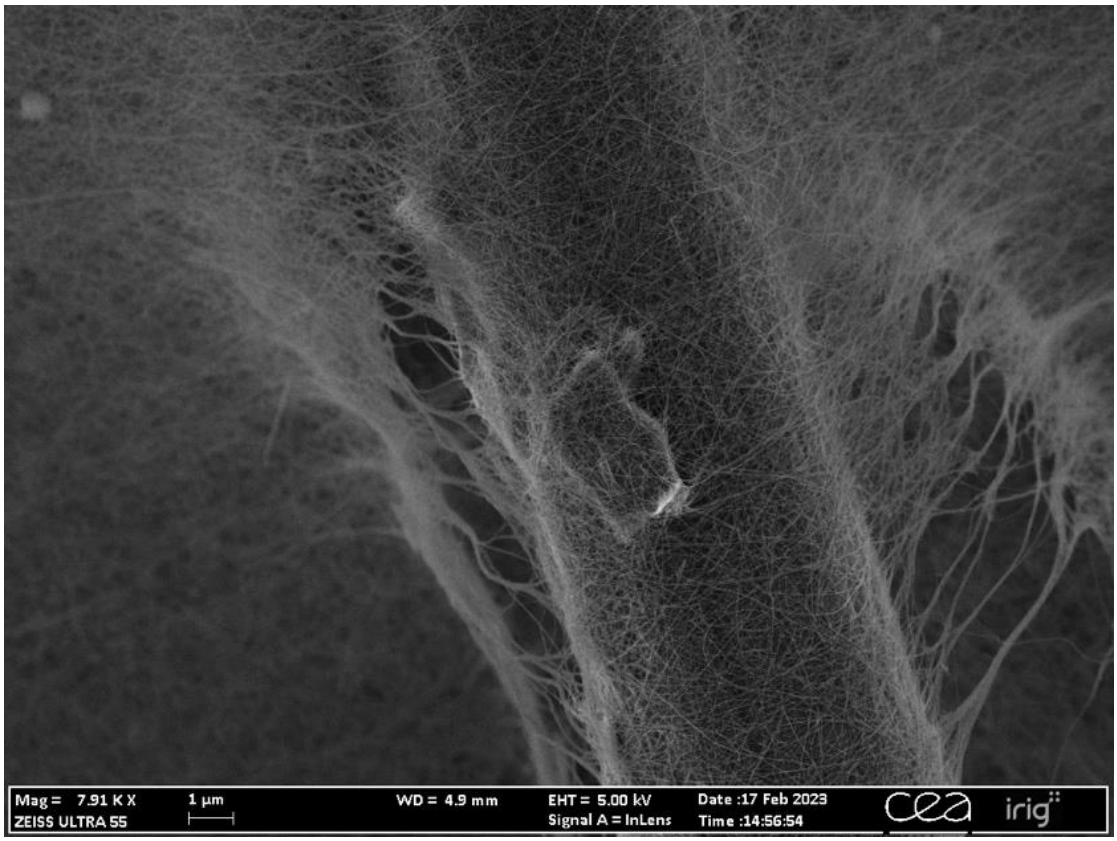

Figure S6.1 Silicon nanowires grown from $CuInS_2$ seeds. Silicon nanowires were grown on a porous carbon gas diffusion layer.

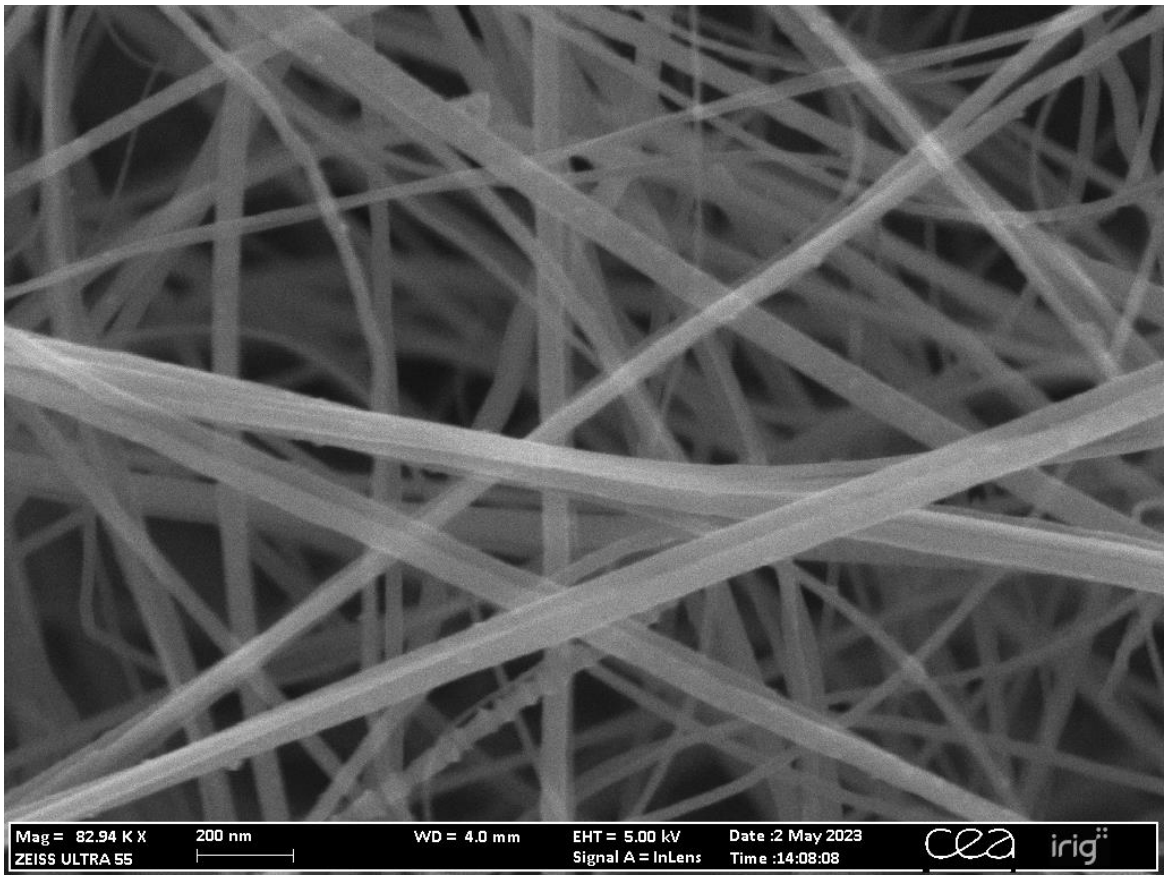

Figure S6.2. Silicon nanowires grown from CuInZnS seeds. Silicon nanowires were grown on a porous carbon gas diffusion layer.

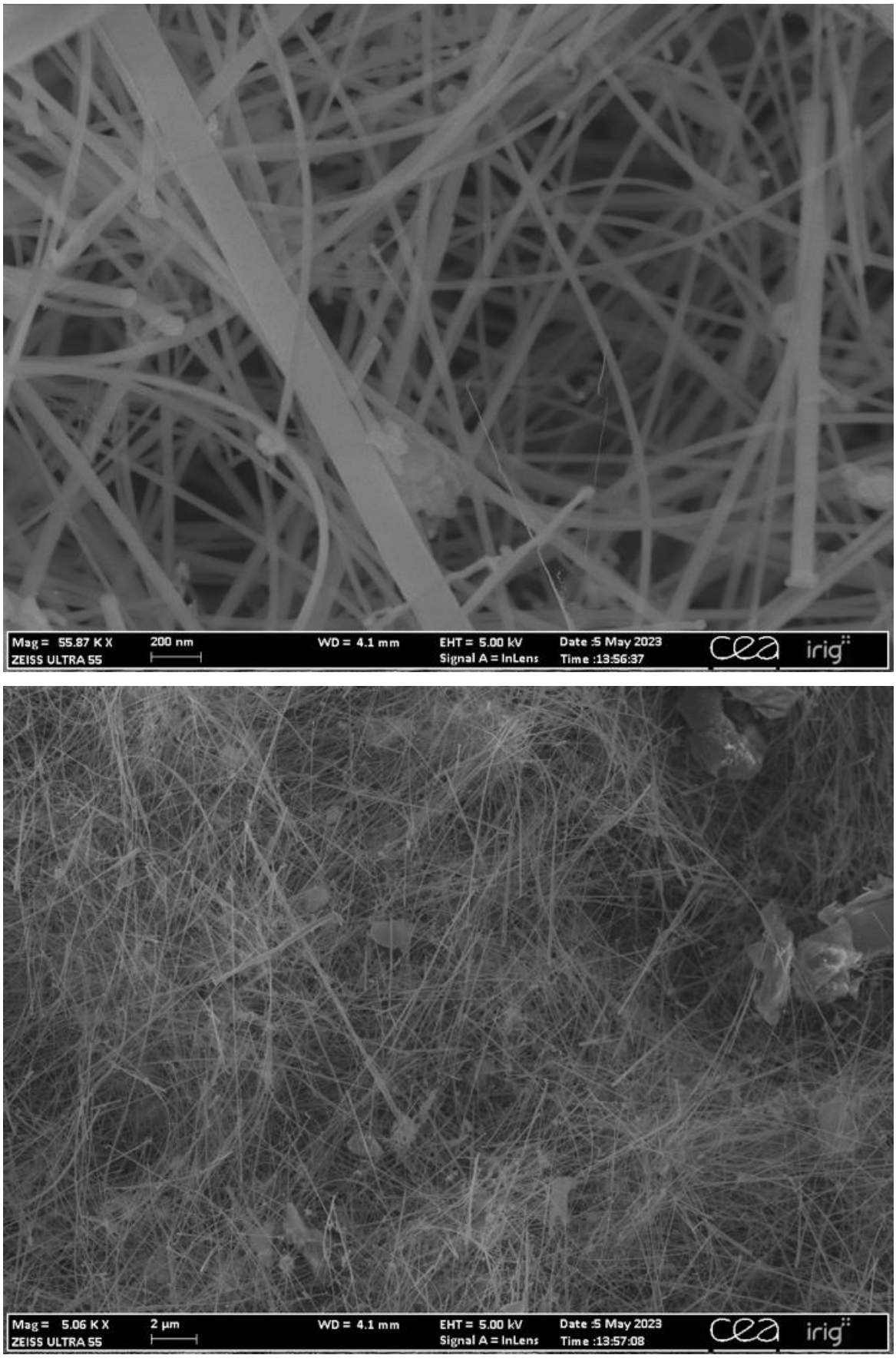

Figure S6.3 Silicon nanowires grown from CuS seeds. Silicon nanowires were grown on a porous carbon gas diffusion layer.

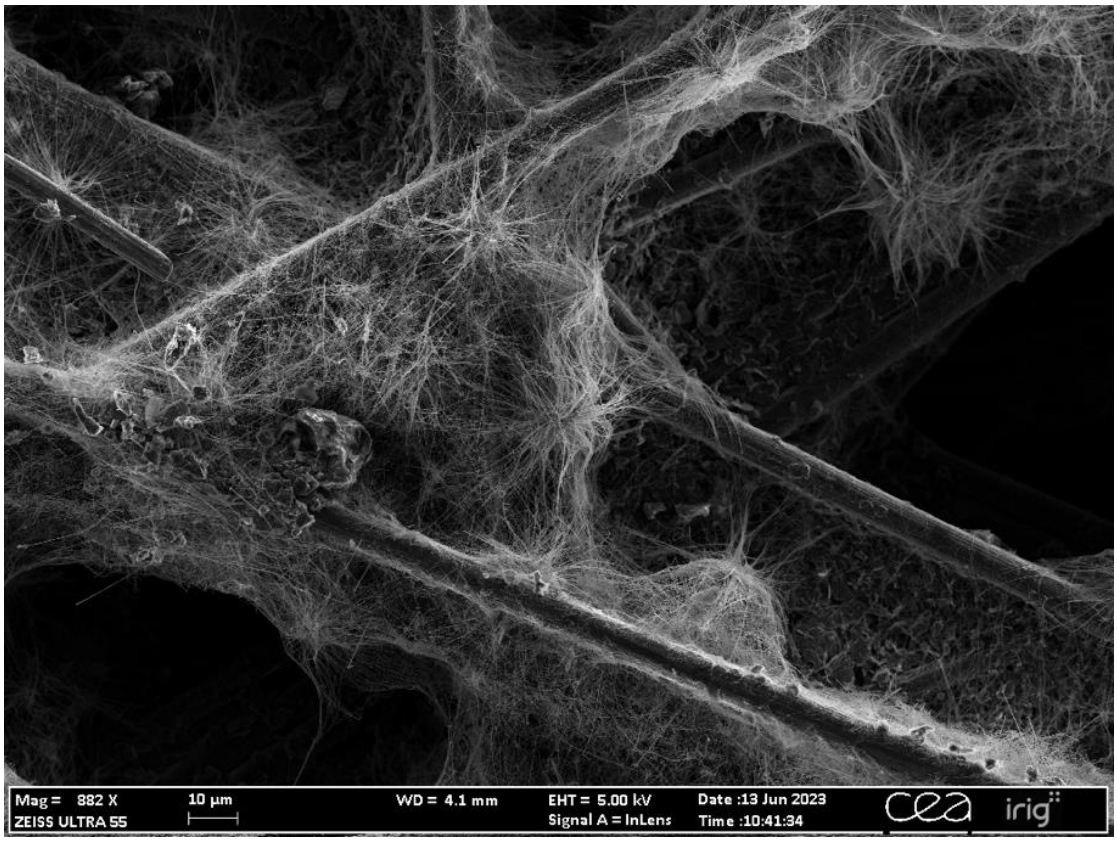

Figure S6.4 Silicon nanowires grown from CuS seeds after degradation of seeds. Silicon nanowires were grown on a porous carbon gas diffusion layer.

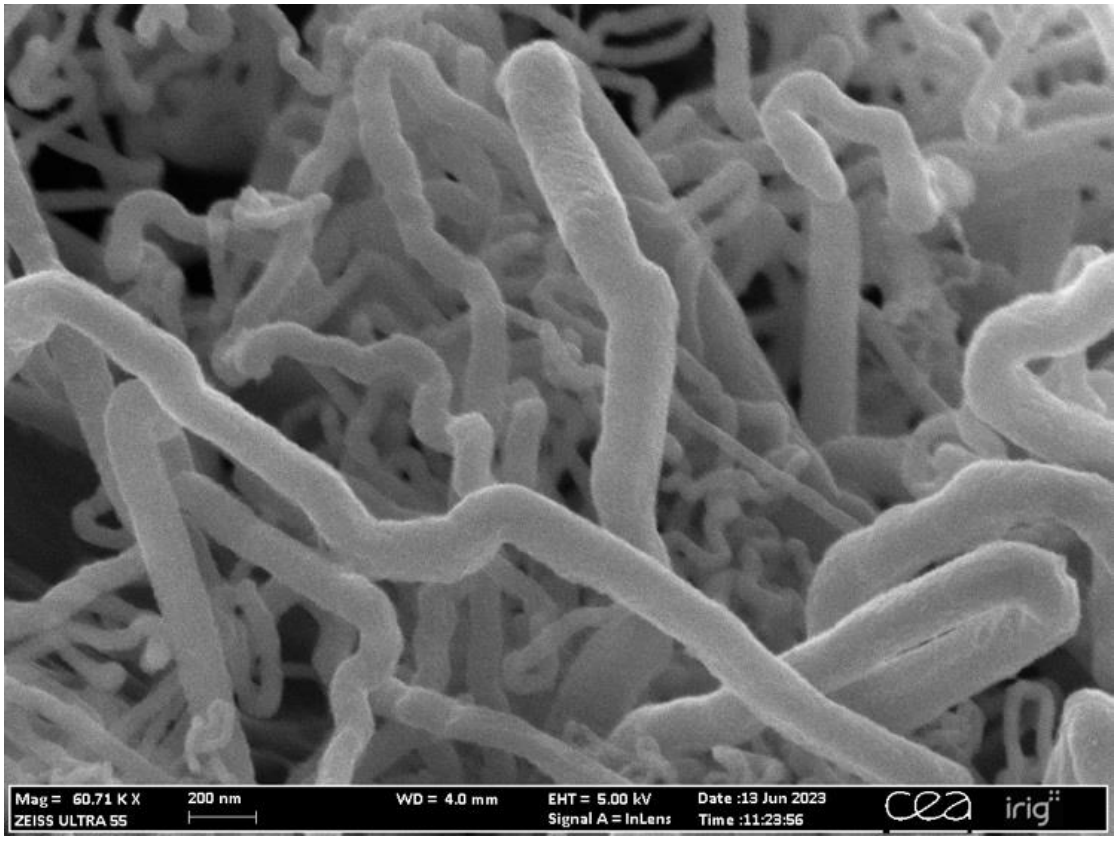

Figure S6.5 Silicon nanowires grown from In_2S_3 seeds. Silicon nanowires were grown on a porous carbon gas diffusion layer.

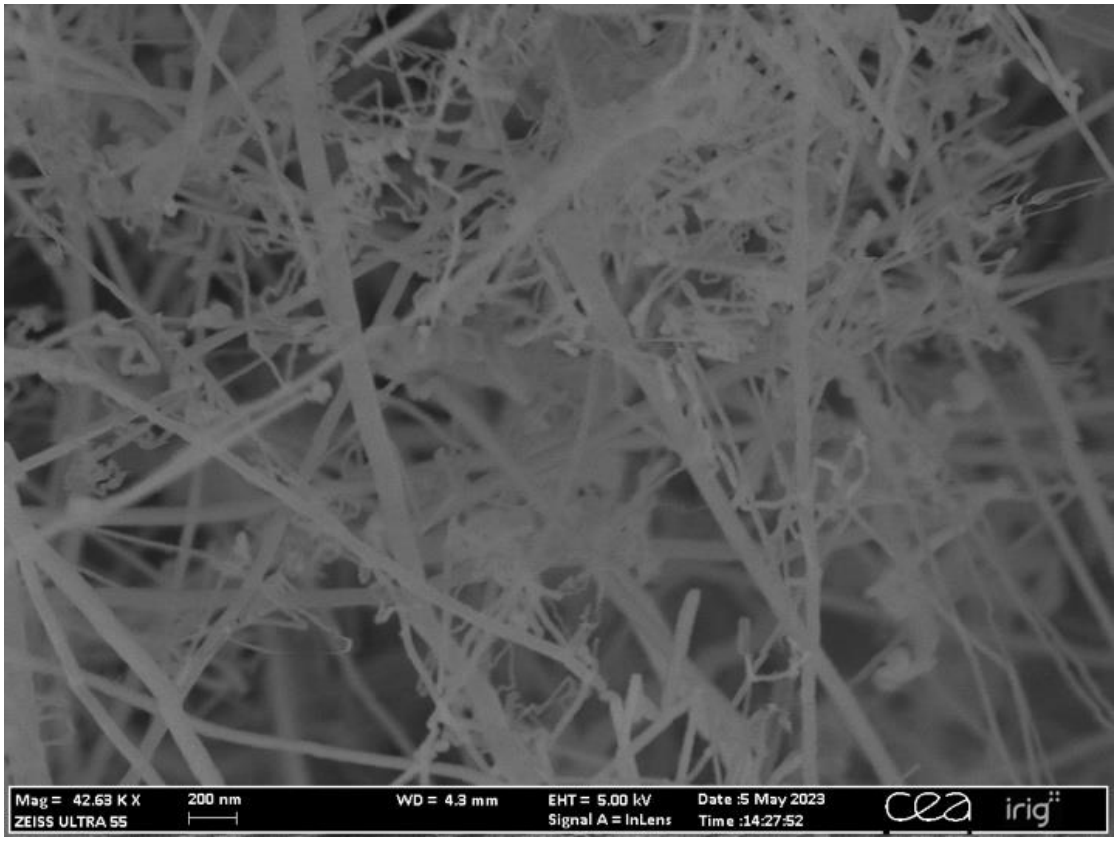

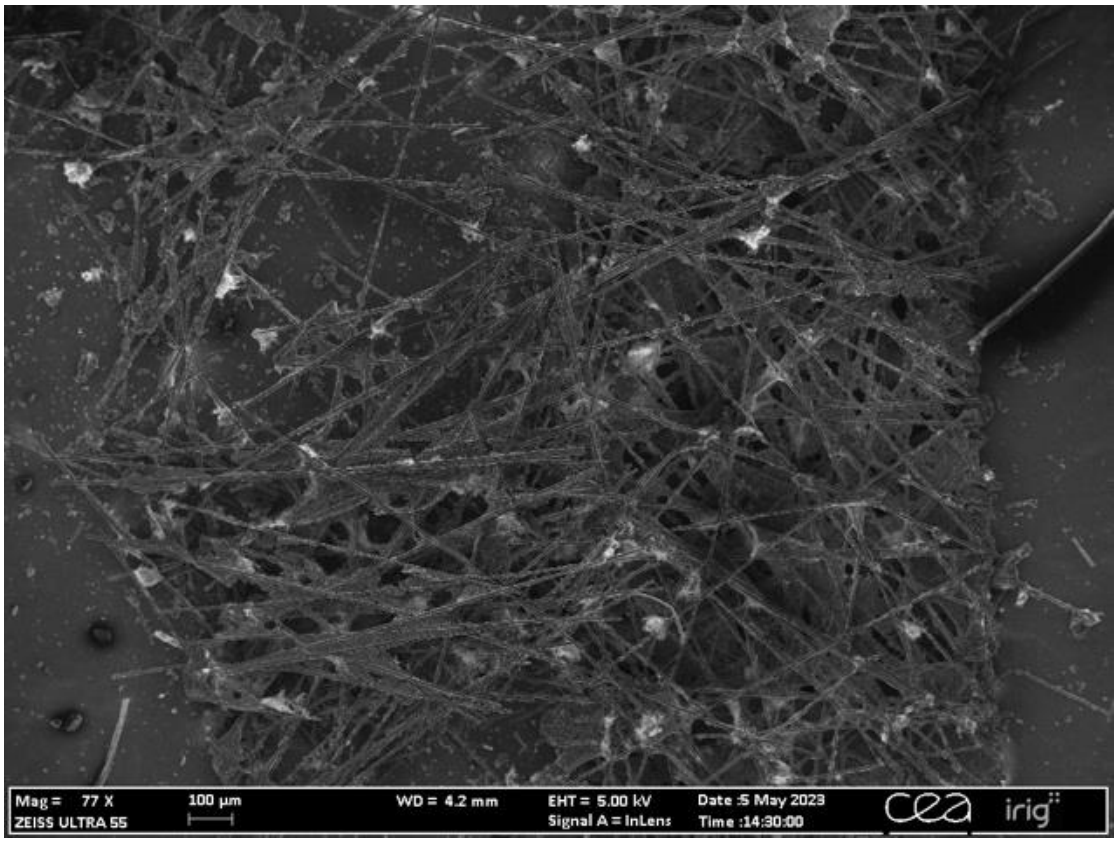

Figure S6.6 Silicon nanowires grown from CuZnS seeds. Silicon nanowires were grown on a porous carbon gas diffusion layer.

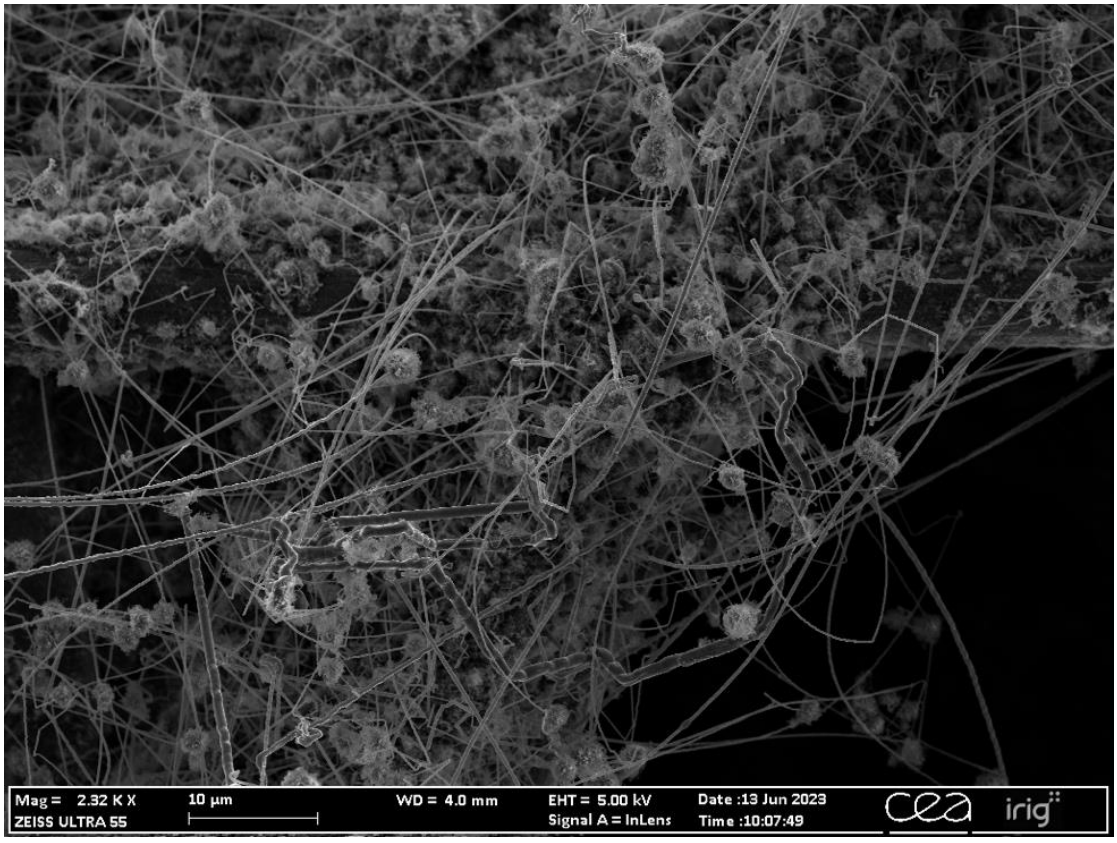

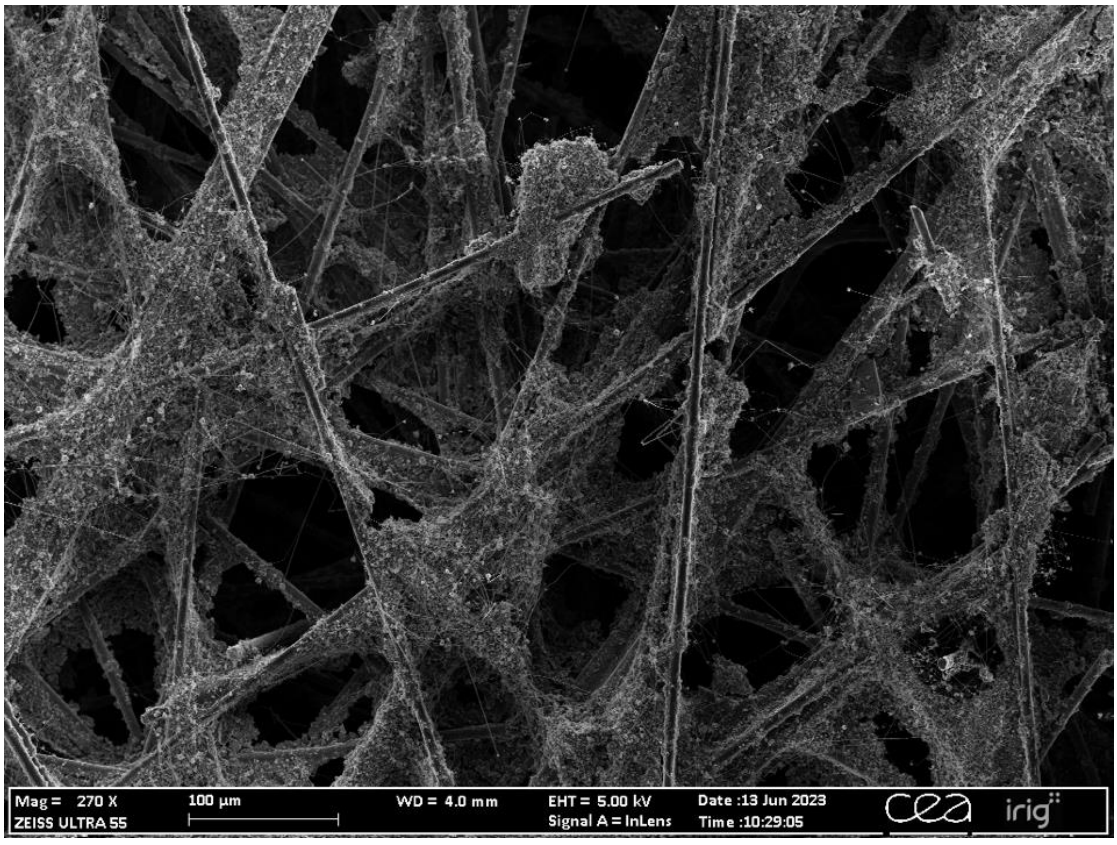

Figure S6.7. Silicon nanowires grown from AgSnS seeds. Silicon nanowires were grown on a porous carbon gas diffusion layer.

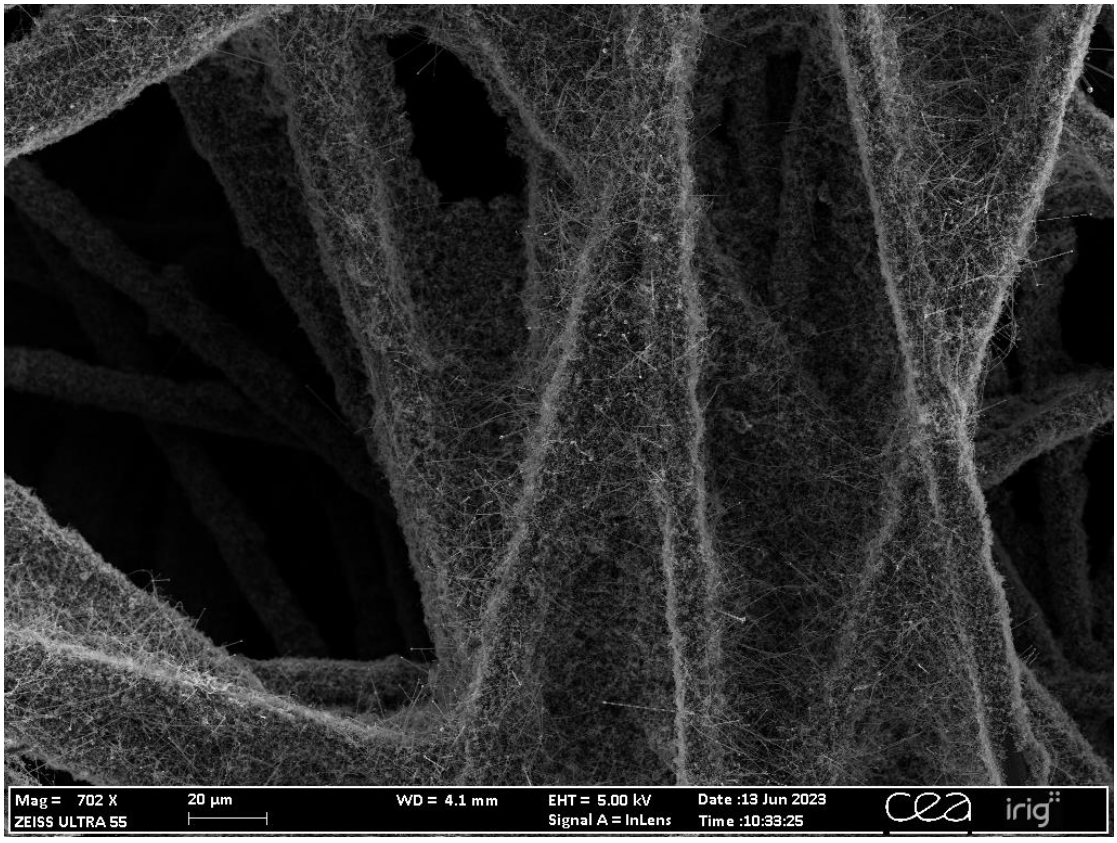

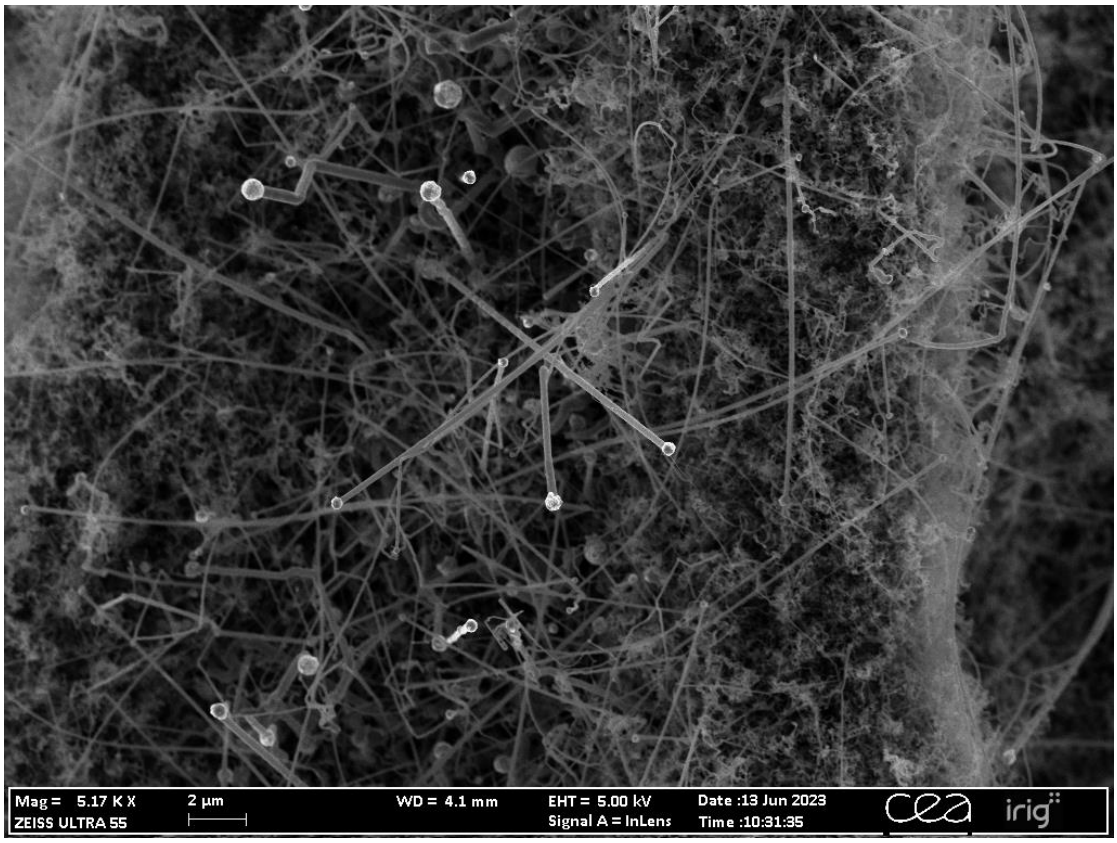

Figure S6.8 Silicon nanowires grown from AgSnZnS seeds. Silicon nanowires were grown on a porous carbon gas diffusion layer.

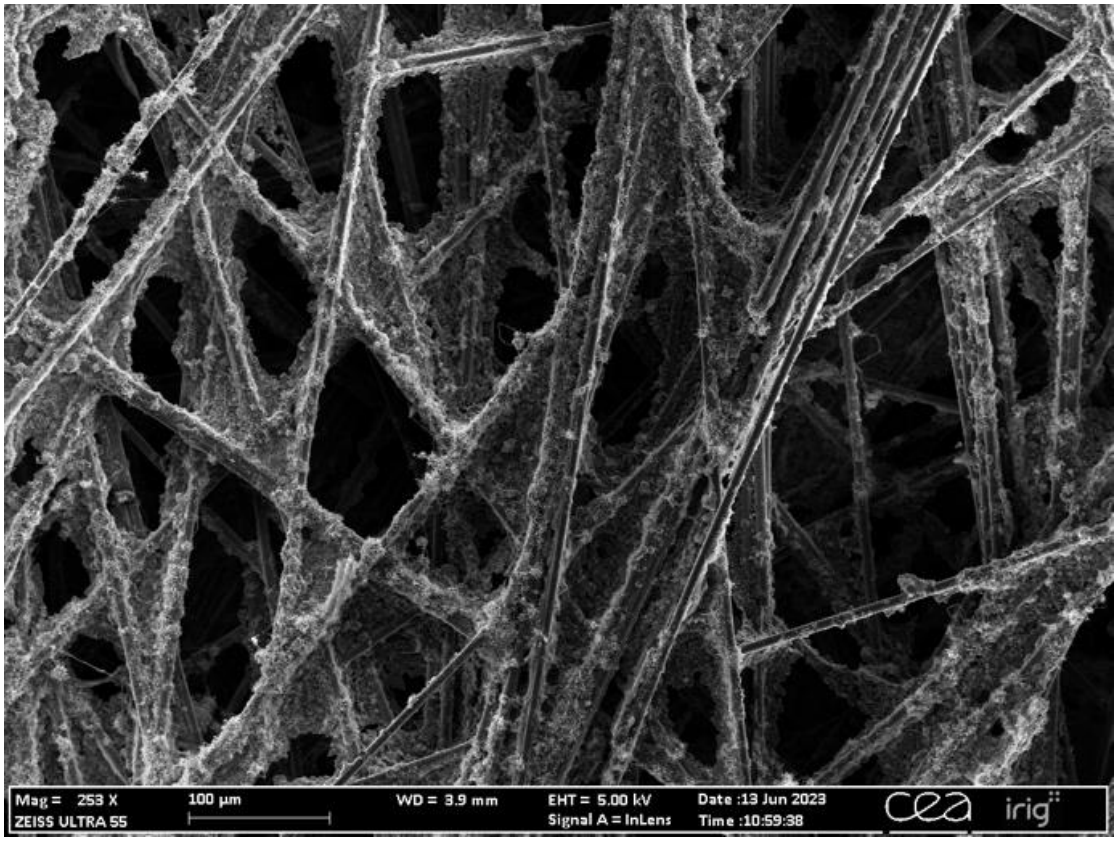

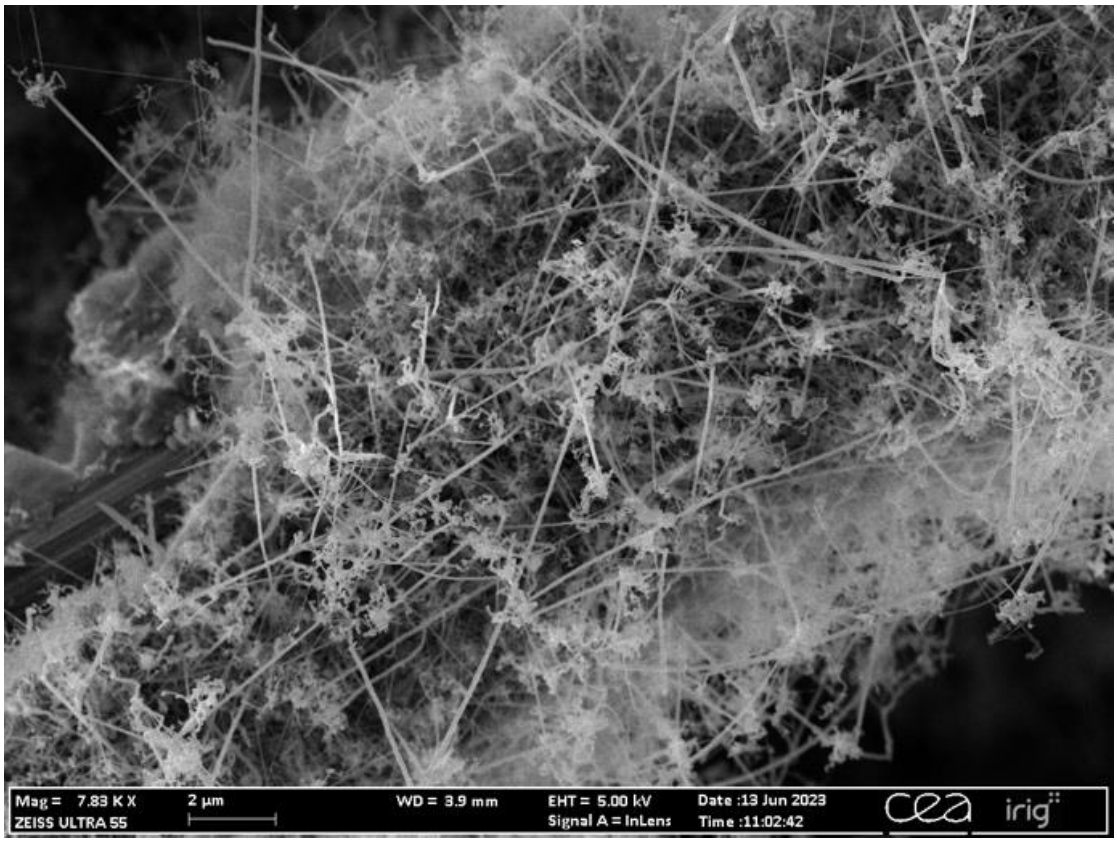

Figure S6.9 Silicon nanowires grown from CuSnS seeds. Silicon nanowires were grown on a porous carbon gas diffusion layer.

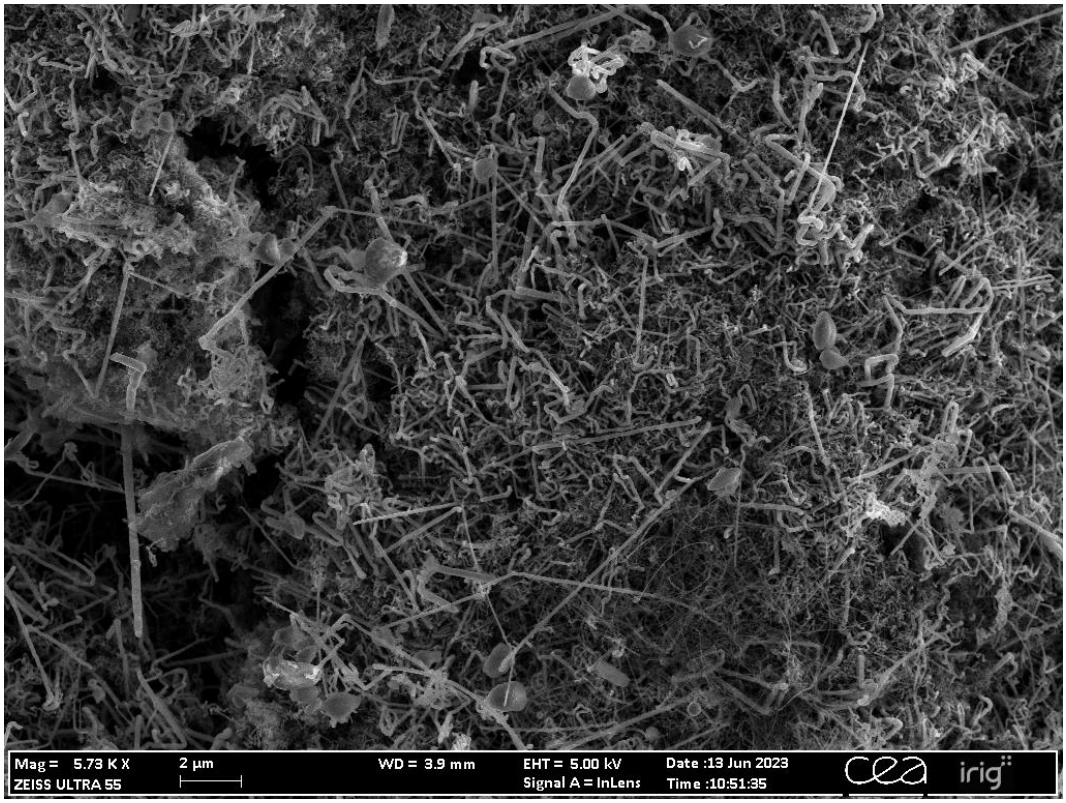

Figure S6.10 Silicon nanowires grown from SnInS seeds.. Silicon nanowires were grown on a porous carbon gas diffusion layer.

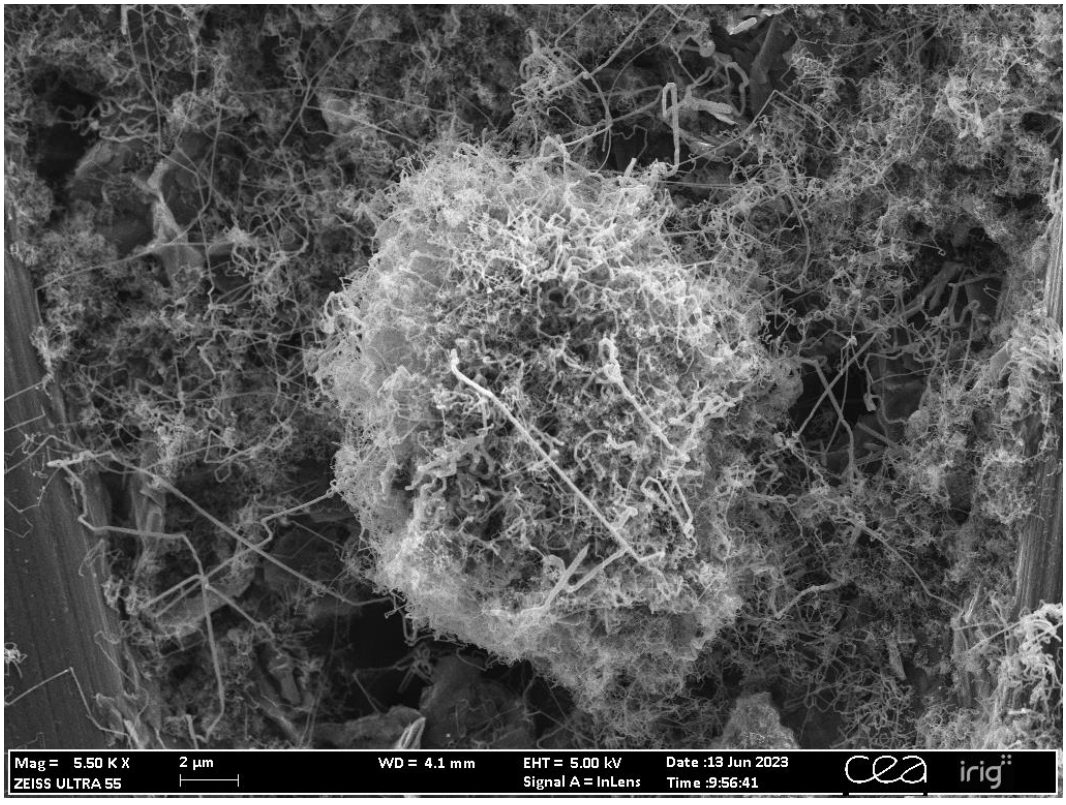

Figure S6.11 Silicon nanowires grown from AgInS:Cu seeds. Silicon nanowires were grown on a porous carbon gas diffusion layer.

Supplementary 7: Synthesis series comparison

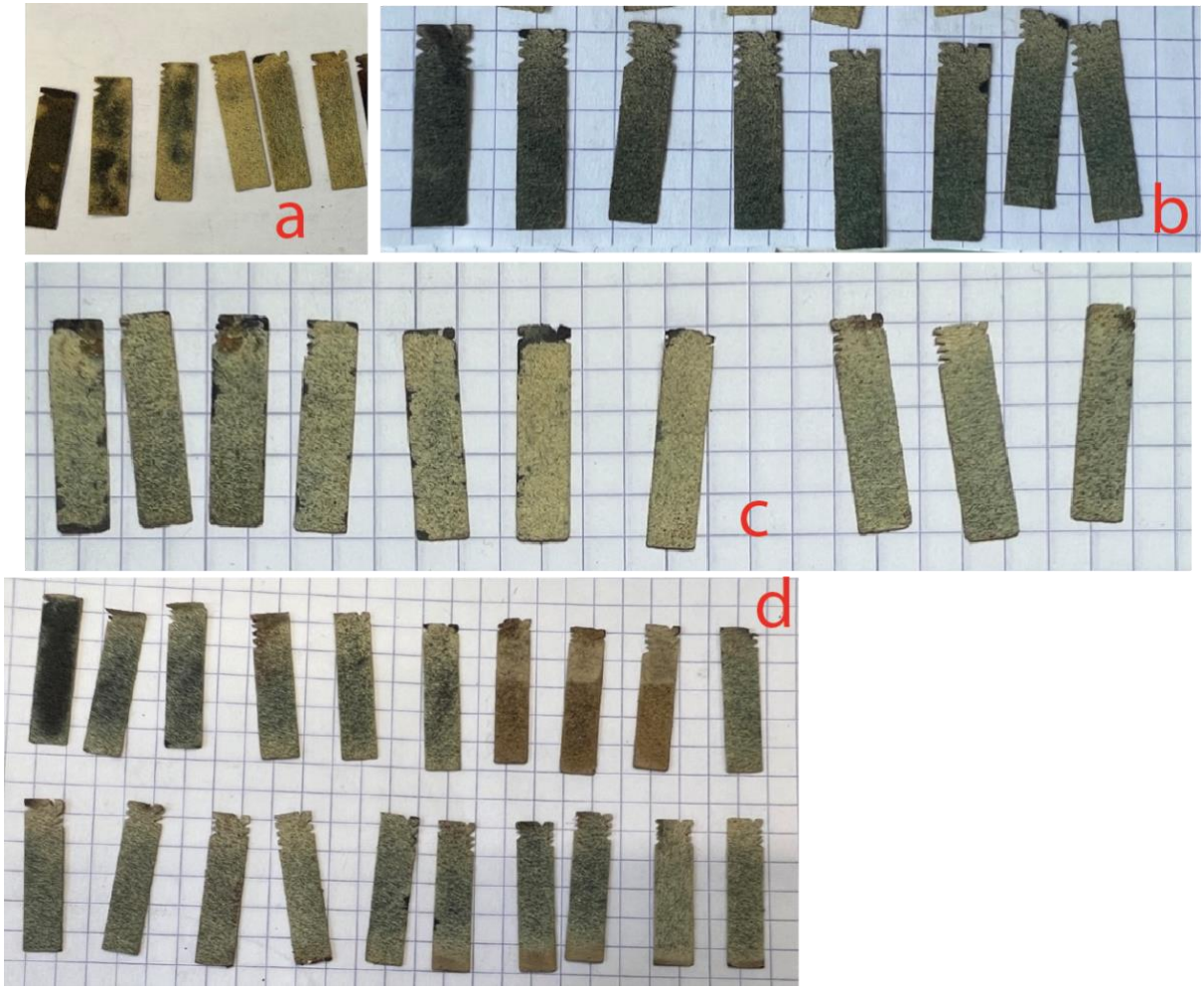

Figure S7. Visual comparison of silicon nanowire growth yield in four different growth series using $CuInS_2$ nanoparticles. Silicon nanowires were grown on a porous carbon gas diffusion layer.

License

Lihtlitsents lõputöö reprodutseerimiseks ja üldsusele kättesaadavaks tegemiseks

Mina, Paul Erik Olli,

1. annan Tartu Ülikoolile tasuta loa (lihtlitsentsi) minu loodud teose ”Photoelectrocatalytic Hydrogen Generation at Photocathode Based on Silicon Nanowires Grown from Alternative Seeds”,

mille juhendajad on Pascale Chenevier ja Jaak Nerut,

reprodutseerimiseks eesmärgiga seda säilitada, sealhulgas lisada digitaalarhiivi DSpace kuni autoriõiguse kehtivuse lõppemiseni.

2. Annan Tartu Ülikoolile loa teha punktis 1 nimetatud teos üldsusele kättesaadavaks Tartu Ülikooli veebikeskkonna, sealhulgas digitaalarhiivi DSpace kaudu Creative Commonsi litsentsiga CC BY NC ND 4.0, mis lubab autorile viidates teost reprodutseerida, levitada ja üldsusele suunata ning keelab luua tuletatud teost ja kasutada teost ärieesmärgil, kuni autoriõiguse kehtivuse lõppemiseni.

3. Olen teadlik, et punktides 1 ja 2 nimetatud õigused jäävad alles ka autorile.

4. Kinnitan, et lihtlitsentsi andmisega ei riku ma teiste isikute intellektuaalomandi ega isikuandmete kaitse õigusaktidest tulenevaid õigusi.

Paul Erik Olli

28.05.2024